Measuring the Droplet-Size and Velocity Distributions in Binary Phase Separation

Messung der Tropfengrößen- und Geschwindigkeitsverteilung in Binärer Entmischung

Diplomarbeit
vorgelegt von

Martin Rohloff
aus
Achim

angefertigt
am Max-Planck-Institut für Dynamik und Selbstorganisation
und der Georg-August-Universität zu Göttingen
2011

Contents

1 Introduction

1.1 Rain in a Test Tube?

The process of cloud formation and rainfall is very complex and involves many length and time scales [1]. According to the fourth assessment report of the Intergovernmental Panel on Climate Change (IPCC) the limited scientific understanding of clouds [2] is a major contribution to the uncertainties in climate prediction. An open question is the connection between the diffusive growth of small droplets and the growth by collisions for big droplets [3]. In the crossover range of 10μm - 50μm droplet radius (chapter 15.1. in [4]) the growth by diffusion as well as by collision is small. This time limiting part in the kinetics of the growth of rain droplets is refered to as a bottleneck. It is not clear how the droplets pass this 'bottleneck' in a time scale, which is comparable to the time between cloud formation and the onset of rain. This motivates to study the evolution of the size distribution in a lab experiment under well controlled conditions. We investigate in this work the demixing of a binary fluid induced by a slow continuous change of temperature. Beyond the critical temperature the binary fluid demixes into two phases. The change of temperature causes supersaturation, which leads to nucleation of droplets. These droplets grow and once they are big enough they precipitate towards the phase boundary. This situation is analogous to the formation of water droplets in warm clouds. To point out the similarities to the clouds we consider a parcel of air raising up in the atmosphere, containing a certain amount of water vapour. While moving upwards the temperature decreases and the amount of vapour which can be mixed with the air without condensation decreases too. At a certain height the relative humidity passes beyond 100% and droplets occur. They grow and eventually fall down as rain. For better comparison we make a rough estimate of the temporal change in composition of air and vapour. In a convective cloud one encounters upwind speeds of about $\Delta H/\Delta t = 10\text{m/s}$. The cooling of an air parcel is given by the dry adiabatic lapse rate of about $\Delta T/\Delta H = 1\text{K}/100\text{m}$ (see p.148 in [5]). The saturation of water vapor in the air also changes with temperature. At 10°C the change of the composition is about $\Delta\Phi/\Delta T = 5 \cdot 10^{-4}\text{K}^{-1}$ (see p.132 in [5]). A combination of all these values give a change in composition of 0.2 per hour:

$$\xi := \frac{\Delta\Phi}{\Delta t} = \frac{\Delta\Phi}{\Delta T}\frac{\Delta T}{\Delta H}\frac{\Delta H}{\Delta t} \approx 0.2\text{h}^{-1} \tag{1.1}$$

In our experiments we vary ξ from $0.05\mathrm{h}^{-1}$ to $2\mathrm{h}^{-1}$, which is comparable to the conditions in clouds. We also observe cascades of precipitation appearing in our system within the range of 30 minutes to two hours, which are comparable to the time scales on which a rain cloud can develop and begin to rain. The advantage of our experiment is that it can be performed under well controlled conditions. How many features of a cloud can finally be squeased into our test tube, will be a result of a detailed analysis, which builds upon the foundations set in the present work.

1.2 Demixing of a Binary Fluid – Oscillatory Behaviour

Let us consider a system with two components A and B. The relative amount[1] of component A is denoted with Φ (see figure 1.1). In general the miscibility of the two components depends on the temperature and can be characterized by a phase diagram. In the phase diagram a binodal is the coexistance curve of the two phases in equilibrium. Below[2] the binodal the system is miscible and the two components form one homogeneous phase. In the two phase region above the binodal the system separates into two phases with compositions Φ_r and Φ_l, which lie on the right and left branch of the binodal respectively.

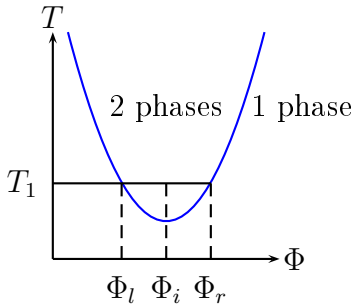

Figure 1.1: Phase diagram of a binary system, the binodal (blue line) separates the one phase region from the two phase region

The amount of each phase can be calculated from these compositions using the lever

[1] This can be volume fraction, mass fraction or molar fraction, if referred to the volume, mass or moles of the components respectively

[2] Here a system with a lower critical solution temperature (LCST) is described, because in this work such a system is experimentally investigated. Only this system is used in all describtions of the phase diagrams to avoid confusions. A system with an upper critical solution temperature is more typical. In this case the system is homogeneous for high temperature, and undergoes phase separation for lower temperatures.

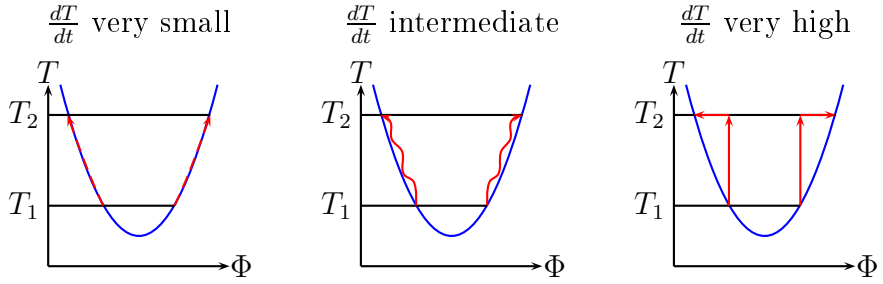

Figure 1.2: Kinetics of the phase separation: a) diffusive case, b) oscillatory demixing, c) temperature jump and relaxation dynamics

rule[3] given an initial composition Φ_i, which is the composition of the homogeneous phase. In the two phase region the composition is fully determined by the temperature. The compositions on the binodal are equilibrium compositions. These description holds for all binary systems, where only one state of matter is considered for each component.
If a temperature change is applied to the system the kinetics become important. Here only liquid systems are considered. We start the in the two phase region, where the binary fluid has already separated into two phases. If there is a density difference between the two phases, they form two macroscopic phases in equilibrium, which are separated by one interface. In figure 1.2 three different temperature changes are shown: a very slow change, a sudden jump and an intermediate change in temperature. Apart from the temperature jump the temperature is changed continuously. First the two extreme cases are discussed. Figure 1.2 c) shows the sudden temperature change where the system is rapidly driven out of equilibrium and the relaxation towards equilibrium, which leads to further demixing can be observed. Depending on the temperature change, spinodal decomposition or the nucleation of droplets and diffusive growth can be observed [6]. In material science sudden temperature changes are often used for alloys to reach an metastable state with desired properties. In this context the phase separation of this kind has been studied in great detail.
The situation is different if the temperature changes very slowly (figure 1.2 a)). The continuous heating produces steadily supersaturation. In order to compensate the generation of supersaturation there is a steady exchange of material through the interface of the two macroscopic phases due to diffusion. This material flux can be described by a nonlinear diffusion equation. The stable diffusion profiles as well as a critical rate of temperature, where these profiles become unstable, has been calcu-

[3]The lever rule is the formulation of mass conservation for this case: the sum of the components A and B in the compositions Φ_r and Φ_l is equal to the total amount of the components in composition Φ_i.

lated [7]. Beyond this stability bound there is the intermediate case (figure 1.2 b)) in which it is more likely for the system to nucleate droplet consisting of the other phase. Here the material does not have to diffuse beyond the interface between the two macroscopic phases. It can just diffuse to the next droplet which acts like a sink for supersaturation. If the two phases do not have the same density, gravity will become important and cause sedimentation of the droplets to the interface. After the droplets have sedimented to the interface of the two phases supersaturation builds up again because the temperature is continuously changing. Beyond a critical supersaturation droplets are nucleated again and the cylcle is repeated. These mechanism leads to an oscillatory behaviour of the demixing of a binary fluid.
The interplay of the two nonlinearities, the diffusion and the coupling of density differences and gravity, lead to an interesting complex dynamics of phase separation. A parameter range in terms of a nondimensional heating rate and a dimensionless gravity parameter of the different regimes are studied in [8]. In the following a parameter range is considered where both the heating rate and the density differences are large enough to yield oscillatory demixing.
The phase seperation dynamics, which show an oscillatory behaviour, first has been described in microemulsions 1997 [9]. These oscillations manifest themselves in turbidity (the light is scattered if lots of droplets are present) and the specific heat. In subsequent studies the oscillatory phase separation has been observed in a mixture of methanol hexane [10], polymer solutions [10], a mixture of vegetable oil and ethanol [11] and butoxyethanol water [12]. Phase separation with a continuous temperature change plays a role in cloud physics [1] or in cooling magma chambers [13].
In figure 1.3 videomicroscopy images, obtained by [12], of the oscillatory demixing process are shown. The light parts correspond to many droplets and dark parts are transparent. In these snapshots the turbidity is not homogeneous. This can be a hint for an advective flow field underlying the whole dynamics. To get a better view on the oscillation dynamics a space time plot from a series of single video microscopy snapshots can be constructed [10] (see figure 1.4). Each image is averaged in horizontal direction, so that a vertical line is left over, which has the width of one pixel. These lines of the vertical turbidity are arranged on a time axis.
Our aim is to examine the oscillatory phase seperation at a length scale of the droplets, see figure 1.5. We want to measure size distributions of droplets, to gain a better understanding of the dynamics of the phase seperation.

1.3 Outline

In the following a short overview of this diploma thesis is given. In chapter 2 the experimental setup is described. It is mainly the work of Tobias Lapp to establish this setup, so only the most important information about the experiment is given.

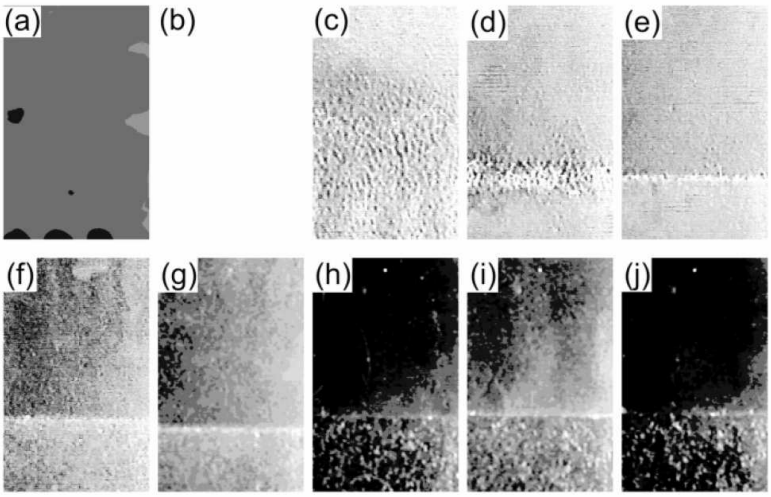

Figure 1.3: The evolution of turbidity in the system butoxyethanol/water. The phase separation is induced by countinuous heating. The homogeneous phase (a), the system at the transition temperature (b), the formation of the two macroscopic phases (c)-(g) and oscillations in the turbidity (h)-(j) are shown, reprinted from [12].

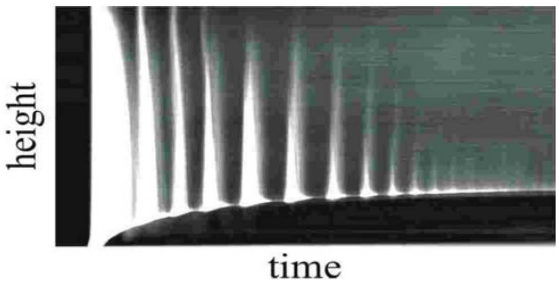

Figure 1.4: Space time plot of the oscillations appearing in a system of methanol/hexane, reprint of [14].

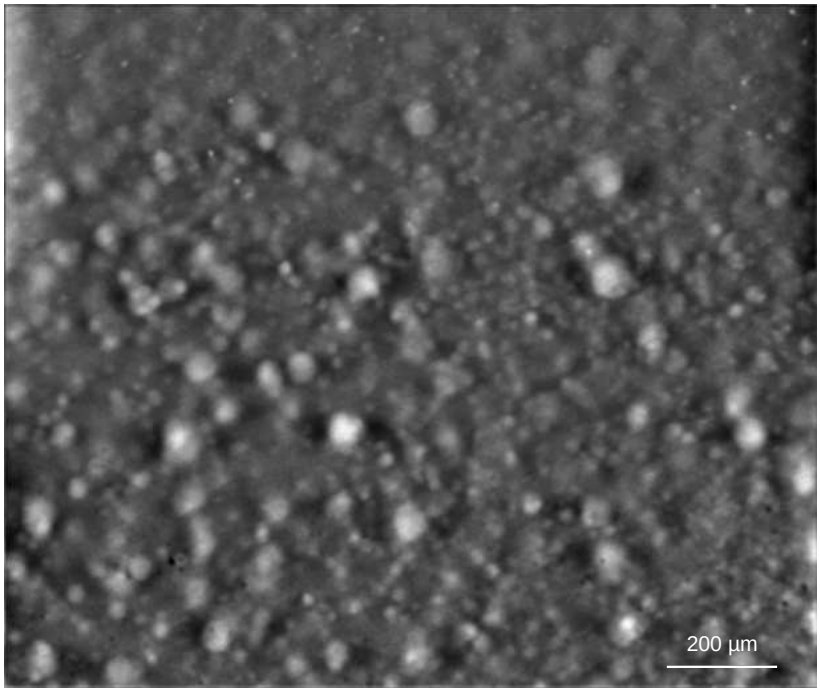

Figure 1.5: Image of droplets appearing in a binary system with a slowly ramped temperature.

In chapter 3 the binary mixture of isobutoxyethanol and water is described, which we use for our experiment to investigate the oscillatory behaviour of phase separation. The material parameters are given and the phase diagram of the system is remeasured to characterize it thermodynamically. To have a constant driving of the phase separation a temperature ramp is calculated, which is adapted to the system. In the experiment images of droplets in a plane are acquired. To get the size distributions from the images the droplets have to be detected. The program which detects droplets in a single image is written by Tobias Lapp. The detected droplets have to be tracked in time to get rid of artefacts and to gain reliable data. This is described in chapter 4.
In chapter 5 the droplet data is analysed. The obtained size distribution of droplets as well as the flow field (accessible from the trajectories) is characterized.
This thesis ends with conclusions in chapter 6.
This thesis is a joint project with the PhD thesis of Tobias Lapp. The work described in the chapters marked with a star (*) is done by Tobias Lapp.

2 Experimental Setup*

Two types of experiments have been carried out. In the first setup the transition temperatures for different compositions of the binary fluid isobutoxyethanol / water are measured to determine the coexistance curve in the phase diagram. In the second type of experiments the binary liquid is exposed to a slow temperature ramp, which leads to demixing. Images of the droplets are taken to study their size distribution and trajectories. Both experiments need a well controlled temperature, as well as a suitable illumination and image aquisition. A sketch of the experimental setup is shown in figure 2.1 [1]. In the following we go through the setup starting with the measurement cells and ending with an image series ready for analysis.

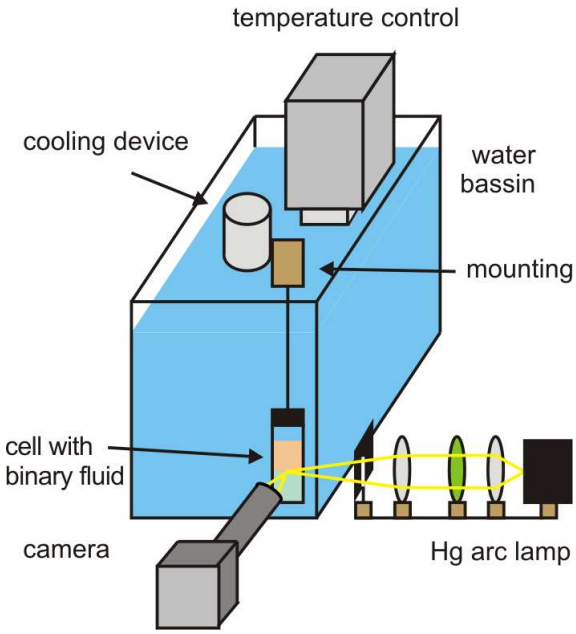

Figure 2.1: Experimental setup for the aquisition of droplet images.

For the measurement of the phase diagram the binary mixture is put into pyrex culture tubes (13mm diameter, 10 cm height). For the droplet measurements we use a fluorescence cell 117.100F-QS made by Hellma GmbH. Its size is 10mm x 10mm and 35mm in height. In both cases measurement cells are sealed with teflon tape

[1] This sketch is drawn by Tobias Lapp.

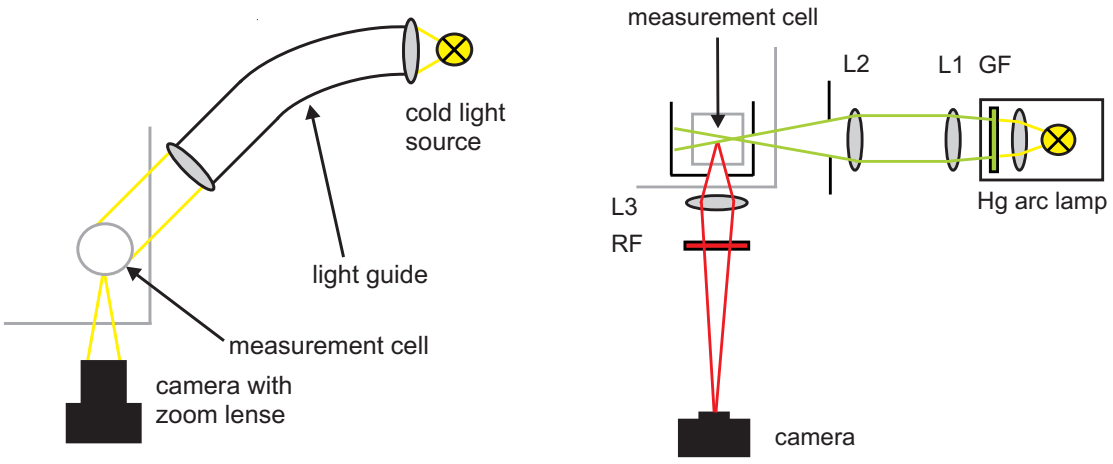

Figure 2.2: Sketch of the optical components of the first (left) and second (right) setup, top view.

and placed in a water bath. The bath is 14cm wide, 34cm long and 16cm high. We use destilled water as cooling agent. The water bath contains a few copper coins to prevent algae from growing.
Underneath the water bath a magnetic stirrer (IKAMAG RET control-visc C) is located. It is used in the first measurement to mix the two phases and to cause turbidity and in the second experiment to mix the two phases after the phase separation. The magnetic stirrer makes it possible to run more than one measurement without unmounting the sample.
The temperature of the water bath is controlled (figure 2.1) by a Haake EK20 immersion cooler combined with a Haake DC30 thermostat. Both parts are immersed in the waterbath. The temperature control unit is connected with the computer via a serial interface. Additionally the temperature of the water near the sample is measured with a PT100 temperature sensor. The water in the water bath is circulating to ensure a spatially homogeneous temperature distribution.The main difference between the two setups are the optical components for illumination and image aquisition. The optics for the first experiment is depicted in figure 2.2 (left). The light from the cold light source (KL 2500 LCD, Schott) is guided with a light guide to the measurement cell. The light source contains a halogen lamp of 250W, but we only need to run it at the lowest possible power to receive enough light. The images are taken with a BM-500CL monochrome progressive scan CCD camera[2]. It has 5 million pixels resolution (2456 x 2058) and a maximum framerate of 15Hz. In this experiment the images are taken with a zoom lense and have a size of about 5mm.
In the second experiment the fluorescent dye nile red is added to the binary liquid

[2]http://www.jai.com/EN/CameraSolutions/Products/Pages/BM-500CL.aspx

in order to have a better contrast between droplets and backround. Nile red solves preferentially in the isobutoxyethanol-rich phase. In the water-rich bottom phase the backround is relatively dark and the isobutoxyethanol-rich droplets shine bright. In the top phase there are dark droplets on a fluorescent backround. To get enough light from the fluorescent dye the illumination has to be very bright. The cold light source is not powerful enough for this purpose. A laser could provide enough light, but problems due to its coherent light arise. Because the optical densities of droplets and the surrounding fluid are not matched, each droplet acts like a small lense. After passing a short distance of the sample the homogeneous parallel laser light is seperated into many stripes, which illuminate the droplets very inhomogeneously. High performance LEDs are also not suitable for the illumination. The power fraction which is emitted with a small divergence angle is not high enough. The optimal light source for the setup turns out to be a mercury short arc lamp from LOT-Oriel 100W. It provides enough light, which is also diffuse enough that almost no stripes appear. The emission line of 546nm and the double line of 577nm and 579nm wavelength[3] are in the excitation band of the fluorescent dye nile red.
A sketch of the optical components is given in figure 2.2 (right). The light is produced by the mercury lamp and is collected by the collimater lense. The light is then filtered with a bandpass filter FF01-562/40-25 by Semrock (green filter GF in figure 2.2) so that only the two green emission lines for the excitation of the fluorescent dye pass. It ensures that the UV light as well as the red part of the spectrum, which overlaps with the emissionspectrum of the fluorescent dye cannot leave the lamp house. A spherical lense (L1) with a focal length of 200mm forms a parallel light beam. The cylindrical lense (L2) with a focal length of 80mm focusses the light in only one direction. With a narrow slit of 300μm width a vertical light sheet is formed which illuminates a plane of the sample. The slit is located in front of the measurement cell already in the water bath. The measurement cell is covered by black apertures to shield strey light. The light comes to the cell through the narrow slit and the fluorescent light leaves through a circular hole in the aperture. The fluorescent light from the illuminated plane of the sample is collected by the spherical lense (L3) with a focal length of 35mm and projected to the CCD-Chip of the camera. A longpass filter (BLP01-594R-25 by Semrock,red filter RF in figure 2.2) is then used to filter out the remaining green excitation light, so that only the fluorescence light passes. The size of the images is 1.3mm x 1.5mm.
The temperature control as well as the camera for the aquisition of the images and the magnetic stirrer are connected with the computer. The whole measurement is controlled by a LabVIEW program. With this highly automatised setup it is possible to run different temperature ramps and take images.
The image processing is done with the Matlab Image Processing Toolbox. To deal with the large amount of data programs are run on a computer cluster. In a typical

[3]http://physics.nist.gov/PhysRefData/Handbook/Tables/mercurytable2.htm, 21.03.2011

measurement we take 20000 images to have a good time resolution, which needs almost 100GB of storage space.

3 Choosing a System

3.1 The Model System

In chapter 1.2 systems which have been used for experiments for the investigation of the oscillatory demixing are mentioned. Our aim was to find an experimental system in which images of detectible droplets can be acquired. Our experiments with a darkfield illumination have shown that the droplets in such images cannot be detected reliably. So we decided to use a fluorescent dye. This fluorescent dye should be dissolved mainly in one phase to give a good contrast between droplets and surrounding fluid. Using polymers seemed to be complicated, but in general it can be a good option to use fluorescent labeled polymers if they can be produced easily. We wanted to stick to a simple system, so we compared the methanol-hexane and the butoxyethanol-water system. The butoxyethanol-water system gives a better contrast, because most of the fluorescent dye solves in a organic compound and not in polar media like water. The disadvantage of this system is the critical temperature of about 50°C. It is a lower critical solution temperature, that means, that the mixture is homogeneous below and has to be heated up to undergo phase separation. Performing experiments between 50°C and 80°C is possible with this system, but not convenient. The water of the water bath evaporates faster, because of the higher vapor pressure. This is not suitable for longterm and automatized measurements. Small amounts of decane will lower the critical point to about 25°C. We tried to measure the phase diagram of a butoxyethanol-water-decane mixture, with 1.6% decane. It turned out that by adding the decane not only the critical point is shifted, but the whole phase diagram is modified. A three phase region appeares [15] and all advantages of a simple phase diagram are gone.
Our final solution is an isomer of butoxyethanol which is called iso-butoxyethanol. It has similar properties, but the critical temperature of a binary mixture with water is about 25°C.

3.1.1 Iso-Butoxyethanol

Butoxyethanol is a organic solvent which is used in many industrial processes and consumer applications[1]. It is part of the important class of nonionic surfactants

[1] Formaldehyde, 2-Butoxyethanol and 1-tert-Butoxypropan-2-ol IARC Monographs on the Evaluation of Carcinogenic Risks to Humans, 2006, 88 ;

which are called n-alkyl polyglycol ether ($CH_3(CH_2)_{i-1}(OCH_2CH_2)_jOH$), abbreviated with C_iE_j. Butoxyethanol is the simplest compound and is denoted in this terminology as C_4E_1 [16]. Iso-butoxyethanol (in the following denoted with i-BE) is a branched isomere of butoxyethanol. Its chemical formula is $C_6H_{14}O_2$.
In figure 3.1 [2] the molecular structure of i-BE is shown.
The i-BE used for this work is purchased from Wako Chemicals GmbH and used without purification.

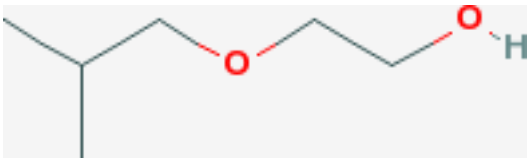

Figure 3.1: Molecular structure of i-BE

3.1.2 Fluorescent Dye Nile Red

As a fluorescent dye we use nile red. It solves in organic compounds where as in water the fluorescence is quenched [17]. Therefore, the i-BE rich phase shines bright and the water rich phase stays relatively dark. Since we do not have pure components in each phase, the contrast between dark and bright parts in the images (taken during one measurement) depends on the composition of the two phases. The more the phases of the system are separated, the higher the contrast.
The excitation spectrum as well as the emission spectrum of nile red depend on the solvent [18]. Nile red solved in butoxyethanol absorbs in the wavelength range of 500nm to 590nm (green light). The emission spectrum has a range of 580nm to 700nm (red). These spectra are measured with a sprectrometer of the type USB650 Red Tide[3] (Ocean optics). It has 2nm spectral resolution. In figure 3.2 the molecular structure of nile red is shown.
The nile red used in our experiment is purchased from Sigma-Aldrich.

3.2 Properties of the System

3.2.1 Phase Diagram of the System

The phase diagram of i-BE / water is very simple. It is a binary system with a miscibillity gap in the temperature region where the measurements take place. To

http://monographs.iarc.fr/ENG/Monographs/vol88/, 23.11.2009
[2]http://pubchem.ncbi.nlm.nih.gov/summary/summary.cgi?cid=521158, 07.03.2011
[3]http://www.oceanoptics.com/Products/usb650.asp, 23.03.2011

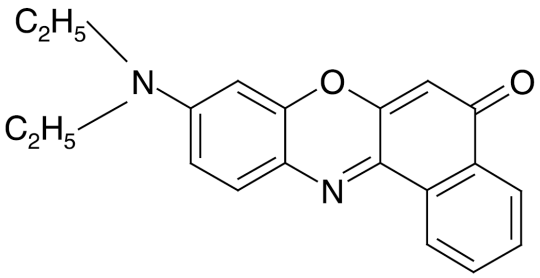

Figure 3.2: Molecular structure of the fluorescent dye nile red, reprinted from [18]

visualize the temperature-dependent existence of the two phases, the equilibrium coexistence curve (binodal) of the two phases is shown in the phase diagram. In figure 3.3 the phase diagram of the system is shown [19]. There is a special feature of this system. The miscibility gap is closed, which means that the system has two critical points. Above the upper critical point (higher than 140°C) and below the lower critical point (25.3°C) the system is homogeneous for all compositions [19]. The fact that the miscibility gap closes for lower temperatures is due to the formation of hydrogen bonds [20] between water and i-BE.

3.2.2 Densities and Viscosities

To understand the sedimentation of the droplets quantitativly it is important to know the density difference between droplets and surrounding fluid as well as the viscosity. In the following, densities and viscosities are calculated for the two phases for all temperatures between 25.8°C and 50°C, which is the measurement range. The change in density is mainly caused by the change in composition. Thermal expansion and excess volume is accounted for based on [21]. For detailled calculation see appendix 2. In figure 3.4 the densities of the two phases and their density difference are shown.
For the calculation of the viscosities we did not find the desired data in the literature. We take the data for the viscosity of water from [22]. The viscosities of i-BE have been measured by Tobias Lapp with an ubbelohde viscosimeter typ 537 10/I made by Schott. The data is fitted with the following function:

$$\eta(T) = A \cdot 10^{\frac{B\cdot(20-T/^\circ\mathrm{C})-C\cdot(T/^\circ\mathrm{C}-20)^2}{T/^\circ\mathrm{C}+D}} \tag{3.1}$$

The coefficients [22] are given in table 3.1.
To interpolate the viscosities for a given composition, the composition-dependent viscosities at 25°C given in [23] are used. The data is interpolated with the following fifth order polynomial (obtained by fitting):

$$\eta(\Phi, \mathrm{T} = 25^\circ\mathrm{C}) = -40.66\Phi^5 + 103.44\Phi^4 - 100.32\Phi^3 + 39.35\Phi^2 + 0.17\Phi + 0.91 \tag{3.2}$$

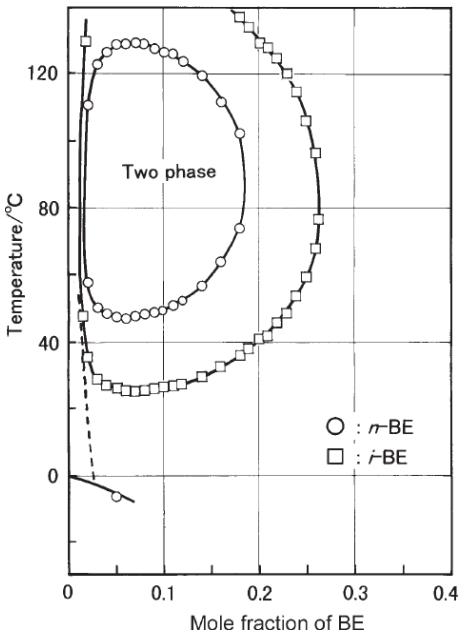

Figure 3.3: Phase diagram of i-BE / water and n-BE / water. Reprinted from [19]

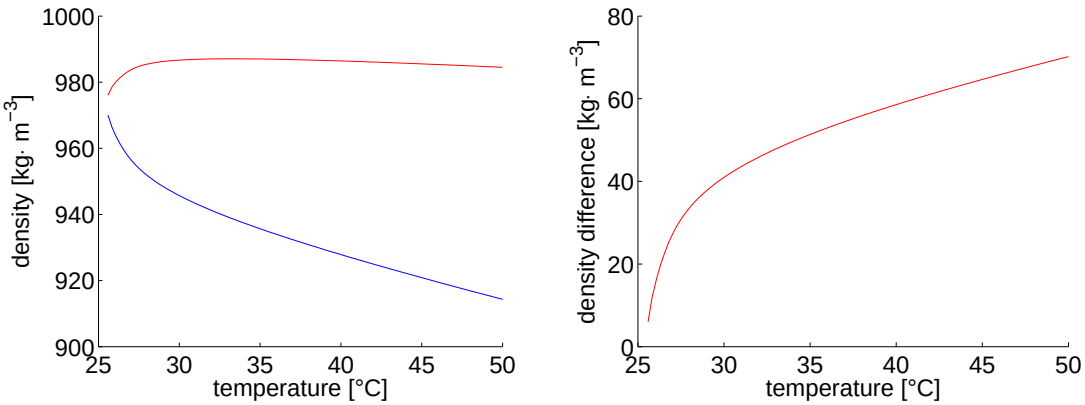

Figure 3.4: Densities of the system i-BE / water as a function of temperature. Left: Densities of the top (blue) and bottom phase (red). Right: Density difference of the two phases.

	A	B	C	D
water	$1.002 \cdot 10^{-3}$kg·m^{-1}s^{-1}	1.3272	0.001053	105
i-BE	$3.36 \cdot 10^{-3}$kg·m^{-1}s^{-1}	1.730	0.001	108

Table 3.1: Fit coefficients for the viscosity of water and i-BE

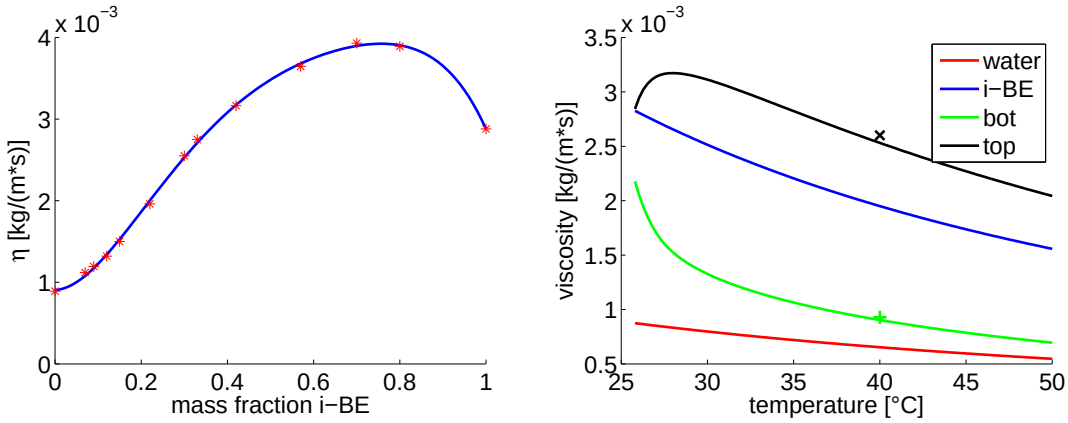

Figure 3.5: Left: Viscosity at 25°C as a function of composition. Right: Viscosities as a function of temperature for water (red), i-BE (blue), the bottom phase (green) and the top phase (black). The two data points at 40°C are measurements of the two phases to test the interpolation.

where Φ denotes the composition in mass fraction and the viscosity η is given in units of kg·m^{-1}s^{-1}. The data and the interpolation is shown in figure 3.5 (left). We now assume that this interpolation curve is not changing in the temperature range of our measurements. Using this assumption we define a rescaled viscosity $\tilde{\eta}(\Phi)$ which only depends on the composition:

$$\tilde{\eta}(\Phi) = \frac{\eta(\Phi, T) - \eta_{H_20}(T)}{\eta_{iBE}(T) - \eta_{H_20}(T)} \tag{3.3}$$

Inserting equation 3.2 gives:

$$\tilde{\eta}(\Phi) = \frac{-40.66\Phi^5 + 103.44\Phi^4 - 100.32\Phi^3 + 39.35\Phi^2 + 0.17\Phi + 0.91 - \eta_{H_20}(T = 25°\text{C})}{\eta_{iBE}(T = 25°\text{C}) - \eta_{H_20}(T = 25°\text{C})} \tag{3.4}$$

The viscosity is hence given by:

$$\eta(\Phi, T) = \tilde{\eta}(\Phi) \cdot \eta_{iBE}(T) + (1 - \tilde{\eta}(\Phi)) \cdot \eta_{H_2O} \tag{3.5}$$

The viscosities of the two phases are shown in figure 3.5 (right) as a function of temperature. For T =40°C we measured the viscosity of the two phases. For both phases it was 2% off the prediction by equation 3.5, which is accuarate enough for our means.

3.3 Measurement of the Phase Diagram

3.3.1 Turbidity Measurements

The turbidity measurements are performed for 25 different compositions in an intervall from 0.10 to 0.67 mass fraction of i-BE. The transition temperature for a composition of 0.10 is about 46°C and for a mass fraction of 0.67 it is 51°C. So in the temperature range from 25°C (critical point) to 50 °C the system is well characterized. This is the temperature range used for the measurements of the droplet size distribution.
For one composition the measuring proceeds as follows: During the whole measurement the mixture with a given composition is stirred with the magnetic stirrer between 300 and 1500 revolutions per minute. The measurement starts above the transition temperature. Here in the two phase region a lot of droplets exist, because the two immiscible phases are stirred. The droplets scatter the light and the system is turbid. The images of the mixture are bright. Then the system is cooled with 35°C/h below the transition temperature. After crossing the transition temperature, the system is in the homogeneous phase and the mixture becomes transparent and the taken images are dark, because no light, except from backround light, is scattered into the camera. Now the system is heated up again with 12 °C/h and at the transition temperature it becomes turbid again. During the changes in temperature, images are aquired with a rate of 1 Hz. The mean grey value of one image is refered to as the turbidity (due to 8 bit grey image the range of the turbidity values is from 0 to 255). In figure 3.6 the change in turbidity for one measurement is shown. From the turbidity plot the time of the phase transition is determined. There is a sudden change in the turbidity when the phase transition happens. To determine the transition, three straight lines are fitted to the turbidity data (red lines in figure 3.6). The intersections of the left and right straight line with the base line give the two transition points. With the temperature logfile the transition temperature is known. The two values for the transition temperature are not the same for heating and cooling the system. This is due to overheating and undercooling and typical for first order phase transitions. The measurement is repeated at least once[4] and the average value of all obtained temperatures is taken for the transition temperature. The standard deviation is considered as the error. At low concentrations of i-BE it is very hard to mix the system properly, because the very tiny i-BE rich phase is located at the top of the sample due to its lower density. The magnetic stirrer stirs at the bottom of the measurement cell. Stirring at 1500 rpm is not efficient enough to mix the whole sample and generate turbidity. In these cases the measurement is modified, so that the sample is only heated up from the homogeneous phase into the

[4]There are also measurments which have been repeated five times, but the differences in temperature for heating and cooling is larger than the differences between single measurements, so we decided that two measurements for each point are sufficient.

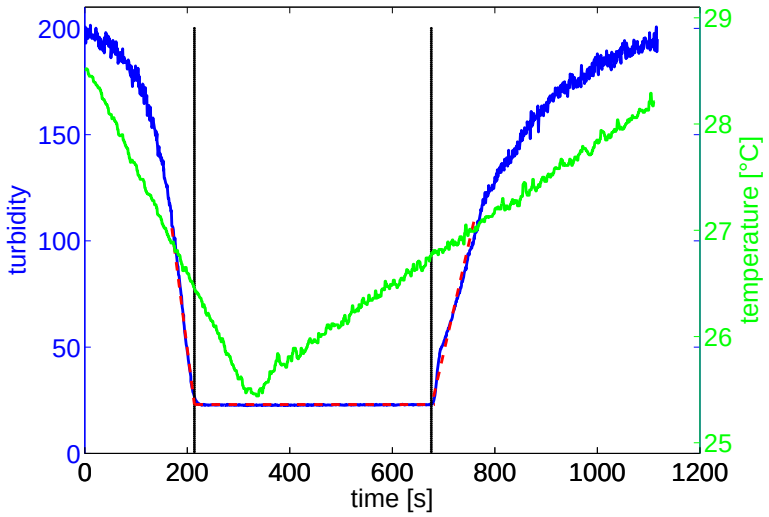

Figure 3.6: Turbidity measurement for $\Phi = 0.20$: the turbidity (blue line) and the temperature (green line) is shown as a function of time. The three dashed red lines are fitted to the turbidity to obtain the transitions (black lines).

two phase region. In this case the turbidity shows a sudden increase at the phase transition.
The measured transition temperatures are shown in figure 3.7. They mark the boundary between the two phase and the one phase region.

3.3.2 Influence of the Dye

The measurements to determine the phase boundary are made without the fluorescent dye nile red, because the turbidity signal is much clearer in this case. There is no fluorescent backround which is present all over the measurement.
For the measurements which are performed to obtain the images of the droplets, the fluorescent dye is needed. So three measurements are performed using a mixture of i-BE, nile red and water, to test if the phase boundary alters. The nile red[5] has been dissolved in 100ml i-BE. From this solution the samples for the turbidity measurements are prepared[6] as well as for all samples for the measurements of the droplet size distribution. There is a good agreement, the data points lie within the errorbars of the other measurements, see 3.7 (red circels). In table 3.2 the transition temperatures are given for the measurements of the data points with and without dye. Therefore we can assume that the fluorescent dye does not influence the phase

[5] We did not determine the amount of nile red, the solution was deep red, and probably near saturation.
[6] which means adding destilled water to gain the desired composition

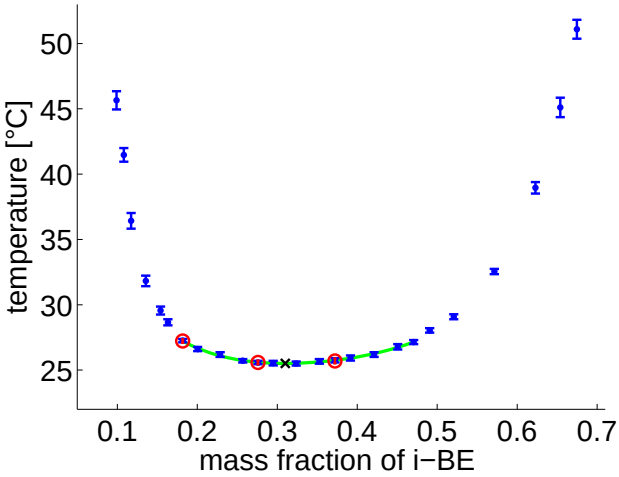

Figure 3.7: Phase diagram of i-BE / water, blue data points correspond to measurements without the fluorescent dye and the three red data points are measurements including the fluorescent dye nile red. The underlying green line is the fit to the data to determine the critical point (black cross).

diagram.

Φ	without dye	with dye
0,18	27.25 ± 0.13	27.23 ± 0.14
0,28	25.58 ± 0.13	25.58 ± 0.14
0,37	25.75 ± 0.17	25.70 ± 0.19

Table 3.2: Transition temperatures for three compositions with and without nile red in units of °C. Within the error the dye does not show any effect on the transition temperature.

3.3.3 Fitting the Phase Boundaries

For the calculation of the temperature ramps the transition temperature has to be known for all compositions in a certain interval. To interpolate the measured data a polynomial fit is used. This fit is performed in two steps. In the first step the critical point is determined and with this the fit of the whole phase diagram is obtained.
To determine the critical point of the phase diagram the data points between $0.18 \leq \Phi \leq 0.47$ are used. A fourth order polynomial in $\Phi - \Phi_c$ is used for the fit, the first

order in $\Phi - \Phi_c$ is set to zero to get a zero slope at the critical point.

$$T(\Phi) = T_c + a(\Phi - \Phi_c)^2 + b(\Phi - \Phi_c)^3 + c(\Phi - \Phi_c)^4 \tag{3.6}$$

The fit is shown in figure 3.7 (green line). The critical mass composition is $\Phi_c = 0.310 \pm 0.004$ and the critical temperature is $T_c = 25.51°C \pm 0.03°C$.
In the second step the two branches of the phase diagram are fitted seperately. To account for the asymmetry of the phase diagram for the right branch a fourth order and for the left a sixth order polynomial is used. Again the first order in $\Phi - \Phi_c$ is set to zero to get a zero slope at the critical point. With this choice the two polynomials give a continuous and differentiable function.

$$\begin{aligned} T_l(\Phi) &= T_c + a_l(\Phi - \Phi_c)^2 + b_l(\Phi - \Phi_c)^3 + c_l(\Phi - \Phi_c)^4 + d_l(\Phi - \Phi_c)^5 + e_l(\Phi - \Phi_c)^6 \\ T_r(\Phi) &= T_c + a_r(\Phi - \Phi_c)^2 + b_r(\Phi - \Phi_c)^3 + c_r(\Phi - \Phi_c)^4 \end{aligned}$$

The parameters of the following fit functions are shown in table 3.3[7] In figure 3.8 the fitted phase diagram is shown.

	left	right
a	51.2	122.2
b	-979.8	-750.7
c	995.3	2574.2
d	120779	
e	647056	

Table 3.3: Fitting parameters of the left and right branch of the phase boundary in units of °C

3.3.4 Comparison with Literature

The phase diagram has already been measured by [19], see figure 3.9. They obtain a critical temperature of 25.3°C and a critical composition of 0.070 molar fraction, which corresponds to 0.331 mass fraction (see appendix for conversion of compositions). These values deviate by $\Delta\Phi = 0.021 \pm 0.004$ and $\Delta T = (-0.21 \pm 0.1)$°C from our measurements. We attribute these deviations to the fact that we are not using purified i-BE as the authors of [19]. Apparently, adding small amounts of dye has an even smaller effect than using different batches of i-BE (see figure 3.7 and table

[7] The coefficients of the higher order terms are high. Since we are only interested in an interpolation of the data points, we do not have to worry about the quality of the fit.

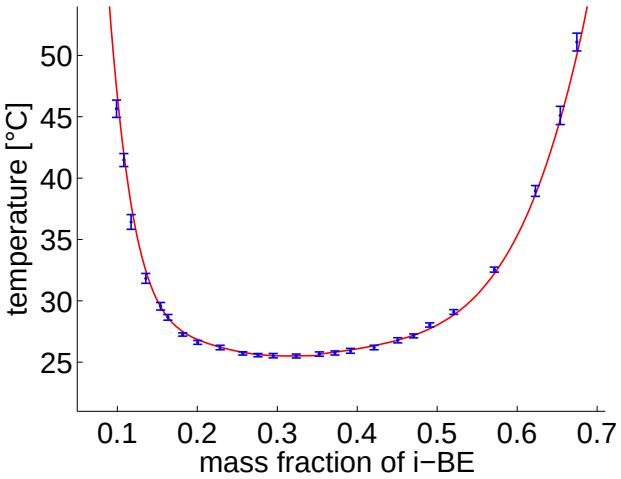

Figure 3.8: Phase diagram of i-BE / water: measured data points (blue) and polynomial fit (red)

3.2). Because of these deviations we remeasure the phase diagram in order to have high precision in the composition data.

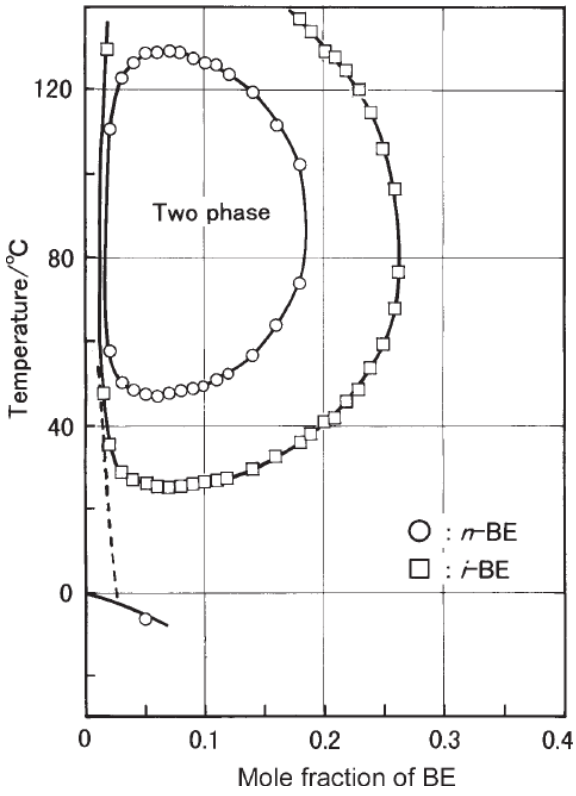

Figure 3.9: Phase diagram of i-BE / water (dots) and n-BE / water (squares), reprinted from [19]

3.4 Constant Thermodynamic Driving

The thermodynamic driving force for the phase separation is the change in composition of the two phases induced by a continuous change of the temperature. To have a better understanding of the response of the system to the driving force we want to keep it constant. In the following we relate the change in composition to the generation of droplet volume. On that basis the driving force can be defined and gets an vivid physical interpretation.

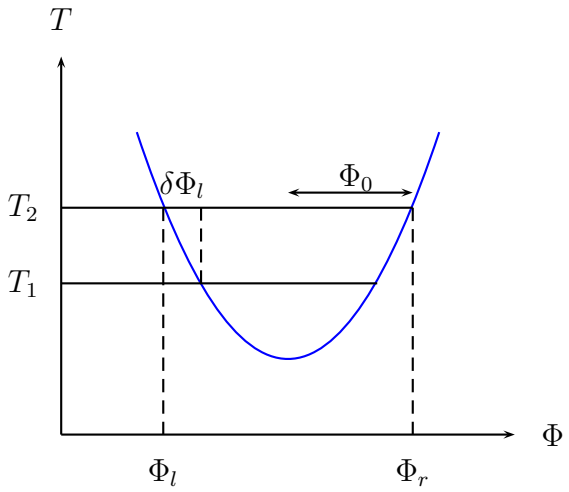

Figure 3.10: Volume conservation of i-BE during a small change of temperature

The *bottom* phase of the demixed system is considered at equilibrium (see figure 3.10). By increasing the temperature slightly from T_1 to T_2, supersaturation (more i-BE in the bulk than in equilibrium) is built up. Because an intermediate heating rate is assumed (chapter 1.2) the diffusive exchange between the two global phases can be neglected. Therefore, the system can only lower its supersaturation efficiently by generating droplets and transporting the i-BE to them. Changes in the densities during this process are neglected. The conservation of i-BE can be expressed with the following equation:

$$V_{bottom}\Phi_l(T_1) = \delta V_{droplets}\Phi_r(T_2) + (V_{bottom} - \delta V_{droplets}) \cdot \Phi_l(T_2) \tag{3.7}$$

The left hand side is the total volume of i-BE which is available in the bottom phase when the system is in equilibrium at T_1. The right hand side describes how the i-BE volume is distributed between the droplets and the bulk at T_2. The composition $\Phi_l(T_1)$ differs from the composition at T_2 by $\delta\Phi_l = \Phi_l(T_2) - \Phi_l(T_1)$.

$$V_{bottom} \cdot (\Phi_l(T_2) - \delta\Phi_l) = \delta V_{droplets}\Phi_r(T_2) + (V_{bottom} - \delta V_{droplets}) \cdot \Phi_l(T_2) \tag{3.8}$$

The compositions now depend on the same temperature and thus the dependence of the temperature will not be shown explicitly anymore. With the introduction of the droplet volume fraction $v := V_{droplet}/V_{bottom}$ and $\delta v = \delta V_{droplet}/V_{bottom}$ for small quantities, the following equation is obtained:

$$\delta v = -\frac{\delta \Phi_l}{\Phi_r - \Phi_l} \tag{3.9}$$

The change in the small quantities happens in the time step δt. Relating the change in the droplet volume fraction δv to the time step δt and going to the limit of infinitesimal quantities gives the following expession:

$$\dot{v} = \frac{dv}{dt} = -\frac{1}{\Phi_r - \Phi_l}\frac{\partial \Phi_l}{\partial t} \tag{3.10}$$

The change in droplet volume fraction is equal to the change in composition divided by the width of the miscibility gap $2\Phi_0 = \Phi_r - \Phi_l$. Performing the same calculation for the top phase leads to an analogous equation for $\dot{v}_{top}$. We define the driving parameter ξ to be equal to the change in droplet volume fraction. Because the phase boundaries are not symmetric this has to be done separately for the bottom and top phase and only one of both can be kept constant in the experiments.

$$\xi_r = \dot{v}_{bottom} = \frac{1}{2\Phi_0(T(t))}\frac{\partial \Phi_r(T(t))}{\partial t} \tag{3.11}$$

$$\xi_l = \dot{v}_{top} = -\frac{1}{2\Phi_0(T(t))}\frac{\partial \Phi_l(T(t))}{\partial t} \tag{3.12}$$

There is also the possibility to keep the sum of both driving parameters constant, this will be used in experiments to control the change of droplet volume fraction in both phases.

$$\xi_0 = \xi_r + \xi_l = \frac{1}{\Phi_0(T(t))}\frac{\partial \Phi_0(T(t))}{\partial t} \tag{3.13}$$

ξ_0 is the driving parameter which is kept constant in experiments by [10]. From the diffusion equation they derived two driving parameters ξ and ζ. They are related to ξ_r and ξ_l as the sum ($\xi = \xi_r + \xi_l$) and the difference ($\zeta = \xi_r - \xi_l$).

3.5 Calculation of the Temperature Ramps

We now want to calculate temperature ramps $T(t)$, which keep one of the three driving parameters ξ_r, ξ_l or ξ_0 constant. In this way the temperature ramp can be adapted to our phase diagram. The equations 3.11 - 3.13 are used as a starting point. The following calculation is done for a constant ξ_r. The change in composition is

proportional to the change in temperature (chain rule), where $\partial\Phi/\partial T$ is the inverse slope of the phase boundaries.

$$\frac{\partial\Phi_r(T)}{\partial t} = \frac{\partial\Phi_r(T)}{\partial T}\frac{\partial T(t)}{\partial t} \tag{3.14}$$

In our experiments we keep the start and end temperature fixed: $T_{start} = 25.8°\text{C}$ and $T_{end} = 50°\text{C}$. By changing the value of the driving parameter the measurement time is changed. Therefore, if the time is rescaled by the measurement time t_{end}, all the temperature ramps for different values of the driving parameter fall on top of each other. The dimensionless time $\tau = \frac{t}{t_{end}}$ is used and substituted in the equation above ($\frac{d\tau}{dt} = \frac{1}{t_{end}}$):

$$\alpha_r = \xi_r t_{end} = \frac{1}{2\Phi_0(T(\tau))}\frac{\partial\Phi_r(T)}{\partial T}\frac{\partial T(\tau)}{\partial \tau} \tag{3.15}$$

For each kind of driving parameter a constant α exists. Using α the duration of the measurement can be calculated and therefore the dimensionless time τ can be converted back into real time.

$$t_{end} = \frac{\alpha_r}{\xi_r} \qquad \text{and} \qquad t = \tau \cdot t_{end} \tag{3.16}$$

The values for $\Phi_r(T)$ and $\Phi_l(T)$ are the data from the measured phase diagram (see chapter 3.3). For the calculation of the temperature ramp the composition is converted to volume fraction (see appendix 1) using the temperature-dependent densities. To integrate equation 3.15 numerically the differential quotient will be discretized:

$$\frac{\partial T(\tau)}{\partial \tau} = \frac{T(\tau+\Delta\tau) - T(\tau)}{\Delta\tau} \tag{3.17}$$

Combined with equation 3.15 an equation for the stepwise calculation of the temperature ramp is obtained:

$$T(\tau+\Delta\tau) = T(\tau) + \frac{\alpha_r 2\Phi_0(T(\tau))}{\left.\frac{\partial\Phi_r}{\partial T}\right|_{T(\tau)}} \cdot \Delta\tau \tag{3.18}$$

With this equation the temperature ramp is calculated stepwise from $T(\tau = 0) = 25.8°\text{C}$ to $T(\tau = 1) = 50.00°\text{C}$. The value of α has to be chosen in a way that the second boundary condition $T(\tau = 1) = 50.00°\text{C}$ is fulfilled. For the integration 10000 uniformly distributed time steps are used.
The equation for ξ_l is analog. For a constant ξ_0 the equations for α_0 and $T(\tau+\Delta\tau)$ are:

$$\alpha_0 = \xi_0 t_{end} = (\xi_r + \xi_l)t_{end} = \frac{1}{2\Phi_0(T(\tau))}\left(\frac{\partial\Phi_r(T)}{\partial T} - \frac{\partial\Phi_l(T)}{\partial T}\right)\frac{\partial T(\tau)}{\partial \tau} \tag{3.19}$$

$$T(\tau+\Delta\tau) = T(\tau) + \frac{\alpha_0 2\Phi_0(T(\tau))}{\left.\frac{\partial\Phi_r}{\partial T}\right|_{T(\tau)} - \left.\frac{\partial\Phi_l}{\partial T}\right|_{T(\tau)}} \cdot \Delta\tau \tag{3.20}$$

The following values for the different α satisfy the boundary conditions mentioned above: $\alpha_0 = 1.61565$, $\alpha_r = 0.99263$ and $\alpha_l = 0.62303$.
In figure 3.11 a) the calculated temperature ramps are shown for the three different cases of $\xi_r = const$, $\xi_l = const$ and $\xi_0 = const$ as a function of the dimensionless time τ. The temperature is changed very slowly in the beginning and relatively fast in the end of the measurement. The increasing heating rate accounts for the increase of the slope of the phase boundaries with increasing temperature. For higher temperatures the heating has to be faster to gain the same change in composition as for lower temperatures. The temperature ramp with $\xi_l = const$ is always below the temperature ramp with $\xi_0 = const$ and the temperature ramp with $\xi_r = const$ is always a little bit above. At the start and end temperature the differences vanish due to the same boundary conditions.
For data analysis and further calculation the time-dependent values of ξ_r and ξ_l for the different driving parameters are needed. They can be calculated easily from the temperature ramp using the defining equations for ξ_r and ξ_l. The formula for ξ_r is given by:

$$\xi_r(\tau) = \frac{1}{2\Phi_0(T(\tau))} \frac{\partial \Phi_r(T)}{\partial T} \frac{\partial T(\tau)}{\partial \tau} \frac{1}{t_{end}} \tag{3.21}$$

The derivative of the temperature ramp $\frac{\partial T(\tau)}{\partial \tau}$ has to be calculated numerically.
In figure 3.11 b) - d) the time dependence of the driving parameters ξ_r and ξ_l are shown for the different temperature ramps. For measurements of a constant ξ_0 the change in droplet volume fraction will increase in the bottom phase (ξ_r increases) and decrease in the top phase (ξ_l decreases) during the measurement (see subfigure b)). For a $\xi_r = const$ the change in droplet volume fraction decreases in the bottom phase (see subfigure c)) and increases in the top phase for a constant ξ_l (see subfigure d)).

3.6 Summary

The binary liquid of isobutoxyethanol and water has a lower critical point at 25.5°C, which allows automatised and longterm measurements. The density and viscosity of the binary liquid are interpolated for all data points of the binodal line. These values are needed to describe the motion of the fluid.
With the measurement of the phase boundaries we have accurate data of the phase diagram of the system, which we are actually using. It seems that the critical point depends on impurities of the used components (c.f. section 3.3.4). From the phase boundaries a temperature ramp is calculated, which keeps the generated droplet volume in one phase constant. With the experimental setup we are now able to take images of droplets forming in the binary fluid, if the temperature is changed due to the calculated temperature ramp.
The temperature ramp starts in the two phase region. After a jump from 24°C,

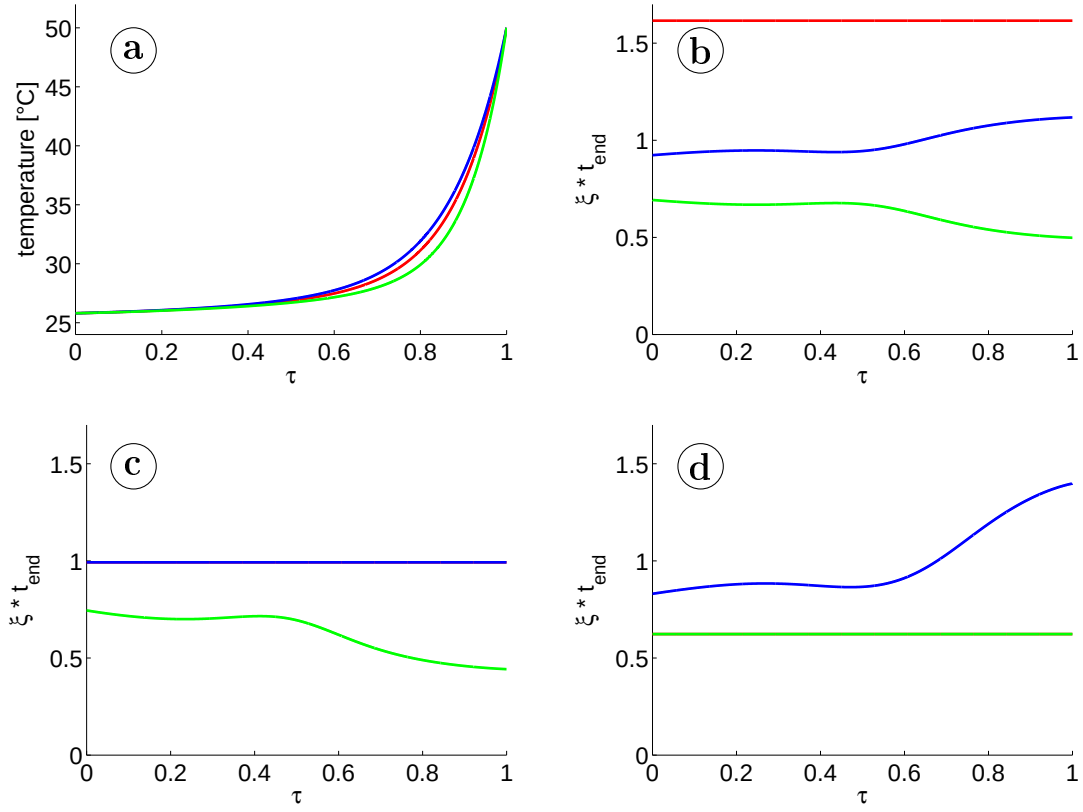

Figure 3.11: Temperature ramps and the driving parameters of the different temperature ramps: a) temperature ramps for the three different constant driving parameters ($\xi_0 = const$ (red), $\xi_r = const$ (blue) and $\xi_l = const$ (green)); b) ξ_r (blue) and ξ_l (green) for a constant ξ_0 (red); c) ξ_l (green) for a constant ξ_r (blue); d) ξ_r (blue) for a constant ξ_l (green).

where the binary fluid is properly mixed in the one phase region, to 25.8°C we wait four hours to let the system relax to equilibrium.
In the next chapter we will see how the droplets in the images can be detected and tracked through the image series.

4 Tracking Droplets

4.1 Motivation

The aim of this chapter is to describe the process which derives a list of droplets (containing position and radius of each droplet) from the gray-value image taken in the experiment. These droplet lists are used for further data analysis, for example to calculate the size distribution.
The first part of this chapter describes how the computer makes a droplet list by processing separate images. Because it is not easy to detect all the droplets properly in an image, the droplets will be tracked through the image series. If the information of the other images is used, the artefacts of the image processing can be reduced: dirt or not properly detected droplets do not have a physical trajectory and can be eliminated. In the second part the droplet tracking process will be described, using the outcoming droplet lists of the processing of single images as a starting point. Here, the water rich phase of the system is considered, where the backround is more or less dark and the droplets are bright. The same algorithm also works in the i-BE rich phase, where the backround is light and the droplets are dark. In this case the images must just be inverted.

4.2 Image Processing of Single Images*

4.2.1 Preprocessing of the Images*

The aim of the preprocessing is to get an image with clearly visible droplets. Without a clear image it is very difficult or even impossible to detect the droplets in the image. To remove artefacts coming from stationary dirt (on the measurement cell or on the camera chip) or inhomogeneities in the illumination, a mean image, calculated from a part of the image series, is subtracted. To reduce the noise and the horizontal stripes in the image it is filtered in the frequency domain using the Fourier transformation. The horizontal stripes are caused by the droplets themselves. The optical densities of droplets and the surrounding fluid are not the same, so the droplets act like small lenses, which give rise to the instationary stripes. To reduce the stripes a high pass filter (gaussian filter with a small width in horizontal and a big width in vertical direction) is used. For reducing the noise a low pass filter (isotropic gaussian filter)

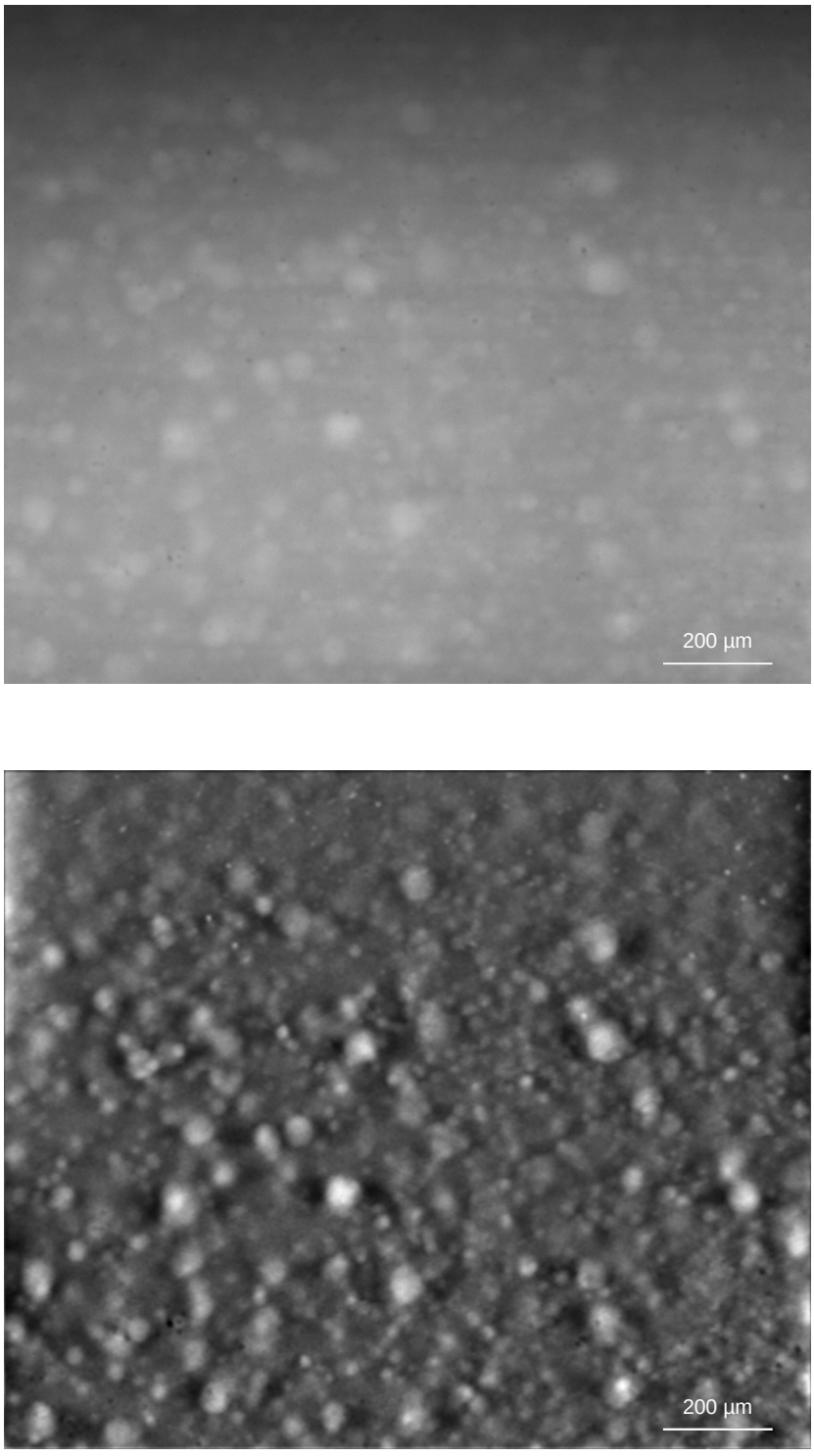

Figure 4.1: Raw image (top) and preprocessed image (below) of a measurement in the bottom phase with $\xi = 1.05 \cdot 10^{-5}$s.

is used. After the filtering the contrast of the image is adjusted. In figure 4.1 the raw image and the preprocessed image are shown.

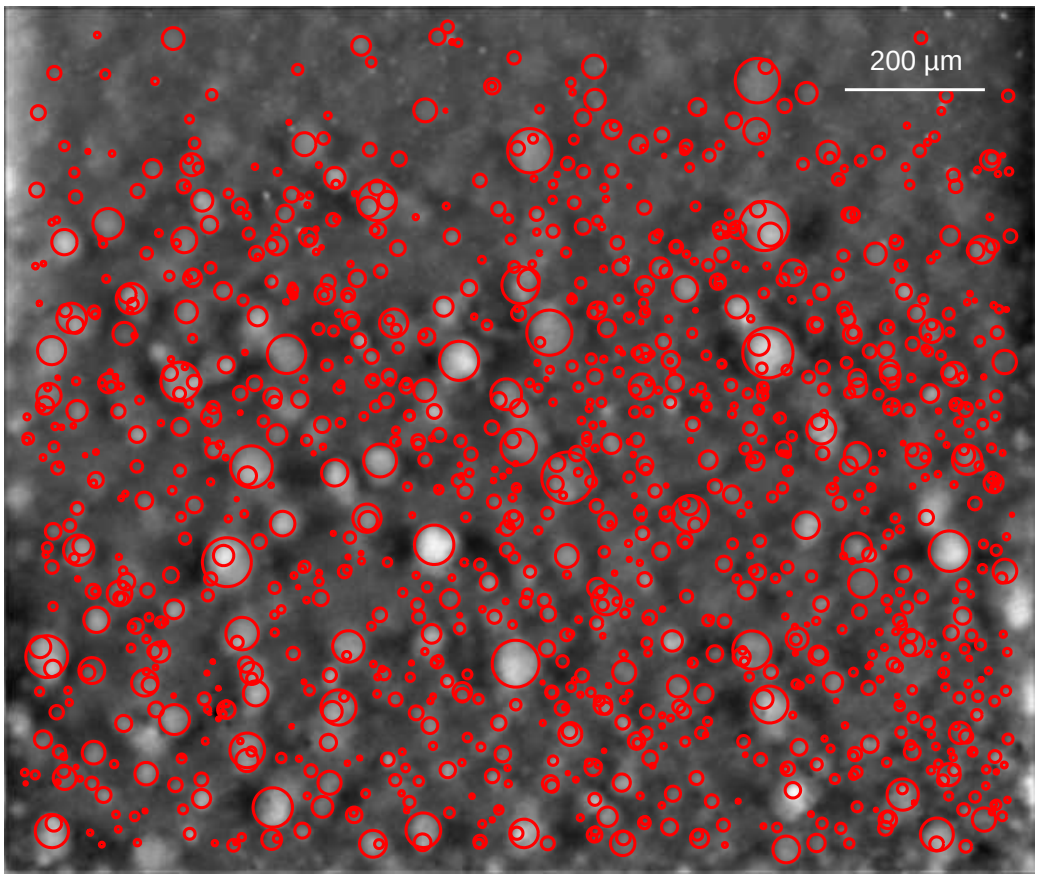

Figure 4.2: Identified droplets in the image of $\tau = 0.1734$ of a measurement in the bottom phase with $\xi = 1.05 \cdot 10^{-5}$s.

To find the droplets in the preprocessed image two steps are made. In the first step rough estimates of droplet radii and positions are obtained. Here methods of image processing like thresholding, edge detection and watershed transformation are used. These estimated values of radius and position are used in the second step. A match function is used to compare the intensity of a droplet $I_{droplet}$ to the intensity of a small ring of 3 pixel around the droplet I_{ring}. If the droplet has the right position and radius the intensity difference should be large, because then the ring covers only dark backround and the droplet only the bright part. The definition of the match function m is given in equation 4.1. The intensity difference is modified with an

empirical radius dependence[1]. x and y denote the position of the droplet and r the radius, they are given in pixel.

$$m(x,y,r) = \frac{1}{30 + \left(\frac{r}{pixel}\right)^{1.3}} \cdot (I_{droplet}(x,y,r) - I_{ring}(x,y,r)) \tag{4.1}$$

For every droplet found in the first step the match with the image is calculated. By varying radius and position of the droplet a local maximum of the match is found. All droplets with a match $m > 0.08$ are considered as droplets. In figure 4.2 all the droplets found in one image are shown.

4.3 Tracking Droplets

4.3.1 Matching the Droplets of Two Images

In chapter 4.2.2 it is described how the droplets can be identified in the images. To track the droplets through a image series the corresponding droplets in consecutive images have to be found. A necessary condition to find these corresponding droplets is that the framerate of the image series is adapted to the dynamics of the droplets. If the droplets are displaced too much between two images they cannot be assigned to each other.
Each droplet of one droplet list is compared to the droplets of the next droplet list. Only the droplets in the surrounding of that droplet have to be taken into account. The droplets, which have the smallest change in position and the radius are matched together. For the identification it is a big advantage that the droplets have different sizes.
In figure 4.3 the matched droplets are shown. The droplets in the image are marked with red circles and the corresponding droplets in the next image with green circles. We observe that the big droplets mainly move upwards. Since an image of the bottom phase is shown, the droplets consist of the i-BE rich phase, which is lighter than the surrounding water rich bulk phase. Therefore the big droplets sediment upwards. The small droplets are advected by the fluid, they simply follow the fluid motion. This observation indicates, that the motion of the droplets has two components: one is the displacement due to the advection of the fluid and the other is the radius-dependent sedimentation due to the density difference of bulk and droplets. A quantitative discussion of this decomposition of the droplet motion is given in chapter 4.4.1.
The matching of the droplets described above uses only the information of the two droplet lists. It can be improved when information of the previous image is also used.

[1] Technical details will be described in the thesis of Tobias Lapp. The match function is given here, because a similar one will be used later.

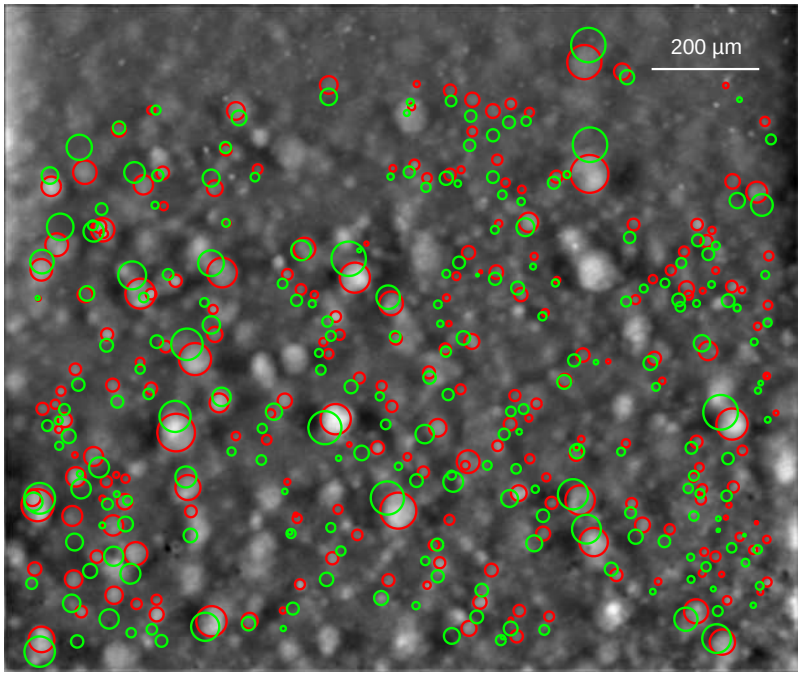

Figure 4.3: Corresponding droplets: the red circles mark the droplets in the background image and the green circles mark their position and radius in the next image.

4.3.2 Calculating the Displacement Field

We now want to use the positions of corresponding droplets in two consecutive images to calculate the displacement. The displacement field is used in the following in terms of the local averaged displacement of droplets due to advection. Hence the displacement due to sedimentation has to be subtracted. A simple assumption for the sedimentation velocity u_{sed} is the Stokes velocity for a sphere of radius r, which is given by the following formula [24](p. 234):

$$u_{sed} = \frac{2}{9}\frac{\Delta\rho \cdot g \cdot r^2}{\eta} \tag{4.2}$$

where $\Delta\rho$ denotes the mass density difference between sphere and fluid, g the gravitational acceleration, and η the dynamic viscosity of the fluid.
To calculate the displacement field the image is divided into sections (25 sections in horizontal direction and 20 in vertical direction). Now the displacements due to sedimentation (see equation 4.2) are subtracted from the displacements of the

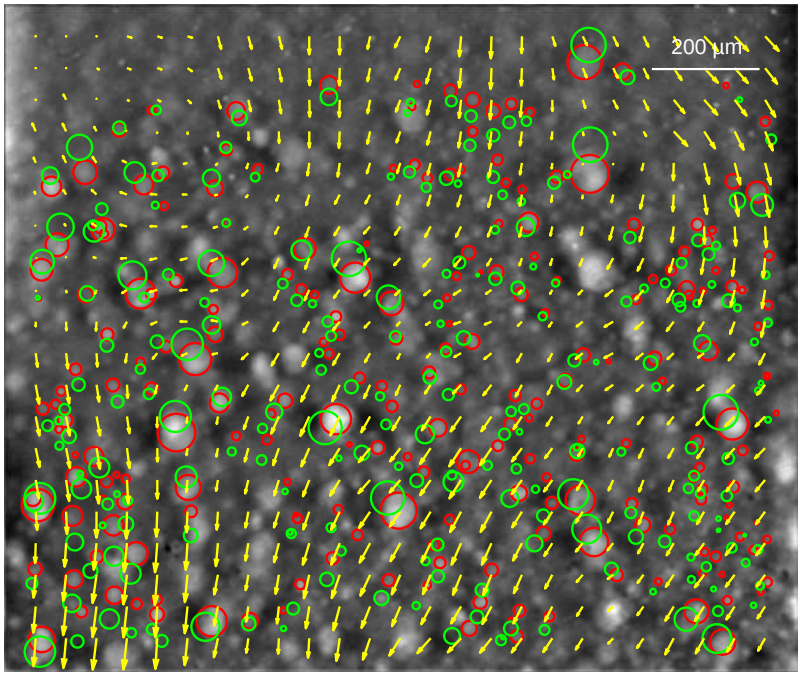

Figure 4.4: Displacement field: the arrows correspond to the displacement of fluid, the red circels mark the droplets found in the image and the green circels their position and radius in the next image. Measurement in the bottom phase, $\xi = 1.05 \cdot 10^{-5}\mathrm{s}^{-1}$, $\tau = 0.1734$.

droplets and the average advectional displacement of all droplets in one cell is calculated. To get a smoother field the four neighbouring cells (at the edges) are taken into account to the averaging process with half weight. This field is smoothed once again with a weighted average taking all the eight neighbouring cells into account with different weights: the original cell has the weight 1/4, the cell with a joint edge gets the weight 1/8 and the four cells in the corners have the weight 1/16. With this process unphysical discontinuities in the displacement field can be eliminated, it has to be smooth because the Reynolds number of the flow is small (in the order of 10^{-1}). The unsmoothed displacement field is also saved and used for further analysis (mean velocities, rms velocities, correlations). In figure 4.4 a smoothed displacement field is shown as well as the matched droplets.

With the displacement field the matching of the droplets of two consecutive images described in chapter 4.3.1 can be improved. We can now add to the position of a droplet the value of the displacement field, calculated with the previous image, at that position and the sedimentation displacement depending on its radius. This new

position can be compared to the droplets in the next image.

4.3.3 Predicting Droplet Positions and Match them to the Image

With the droplet tracking we want to improve the detection of droplets in the images. What is used so far is the information of the droplet lists. We can make some improvements if we use also the information of the previous droplets list. But what can be done if a droplet has not been detected? Here the information of the raw images or the preprocessed images can be used. The main idea is to make a prediction of the droplet position and compare it to the preprocessed image. In the following the algorithm, which tracks the droplets forward in time is described. The different steps are shown in figure 4.5.

The starting point is a droplet of the droplet list of image 1. This droplet (see

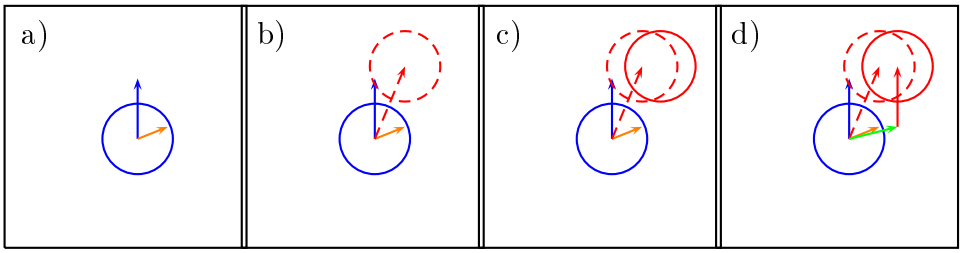

Figure 4.5: Steps of the forward tracking: a) two components of the displacement, b) predicting the droplet, c) matching the droplet to the next image, d) recalculating the advective displacement

subfigure a)) has a displacement due to its sedimentation velocity (blue arrow) and a displacement due to the advection of the fluid (orange arrow). With these two components a position of the droplet in the next image is predicted, the radius stays the same, see the red dashed circle in subfigure b). The predicted droplet is matched to the image 2 using a match function similar to the one described in chapter 4.2.2, see the red circle with the solid line in subfigure c).

It is necessary to modify the match function (see equation 4.1) used for the droplet finding in a single image, because often little droplets are detected at the edge of big droplets. To reduce the number of these cases another term is added to the match function. If a little droplet is located at the edge of a bigger droplet, a little part of its halo is covering the dark backround and the remaining part is covering the relatively light part of the big droplet. If the little droplet is located totally in front of the big droplet these intensity difference will not appear. So the modification takes this asymmetry into account. The intensity weighted centroid of the halo (denoted as x_r and y_r) is calculated. It is compared to the droplet position. The deviation accounts for this asymmetry and should make the match smaller. The

empirical prefactor α is there to balance both parts of the match function given in equation 4.3.

$$m(x,y,r) = \frac{1}{30+(r)^{1.3}} \cdot (I_{droplet}(x,y,r) - I_{ring}(x,y,r)) - \alpha \cdot \frac{(x-x_r)^2+(y-y_r)^2}{r^2} \tag{4.3}$$

The radius r and the coordinates x, x_r, y and y_r are given in pixels. We use $\alpha = 3$. Again radius and position are varied until a local maximum of the match function is found. All droplets with a match $m > 0.08$ are accepted.
Now two corresponding droplets have been found. The advective displacement used for the prediction of the droplet (orange arrow) has been an estimate based on the information of the past. Using the positions of the two corresponding droplets the advective displacement is calculated again subtracting the sedimentation (see green arrow in subfigure d)).
These steps are made for all droplets of the droplet list of image 1. The corresponding droplets of the two images are sorted into trajectories. Then this procedure is repeated starting with the droplet list of image 2 and the additionally found droplets of the tracking step before.
All the matched droplets are sorted into trajectories. The trajectory of a droplet contains all its positions and radius values in the different images. They are saved with an index corresponding to the file index of the image where the trajectory starts.

4.3.4 Enlarge Trajectories

It is sometimes the case, that a droplet is visible in several images but not tracked from the first one. It is also possible, that two trajectories are seperated by a not so clearly visible droplet, which has not been found. To overcome these problems to a certain extent the droplets are also tracked backwards in time. Starting with the trajectories calculated in the forward tracking the beginning of each trajectory is analysed. A sketch of the different steps is shown in figure 4.6. From the displacement field and the sedimentation the droplet position is predicted into the past, the radius stays the same (subfigure b)). This predicted droplet is matched to the previous image with the same match function used in the forward tracking (subfigure c)). Now this matched droplet is compared to a list of all droplets in that image being part of a trajectory. If the droplet agrees in position and radius with a droplet *at the end* of a trajectory, the two trajectories will be fused, so that a hole between two seperated trajectories is filled. If the droplet does not match any droplet in that list, the droplet will be added *at the beginning* of the trajectory, which is thereby enlarged (see subfigure d)). All the other droplets have been matched to a droplet which is already part of a trajectory. They are deleted, so that there are no branches of the trajectories possible. In the whole tracking algorithm the collision of droplets

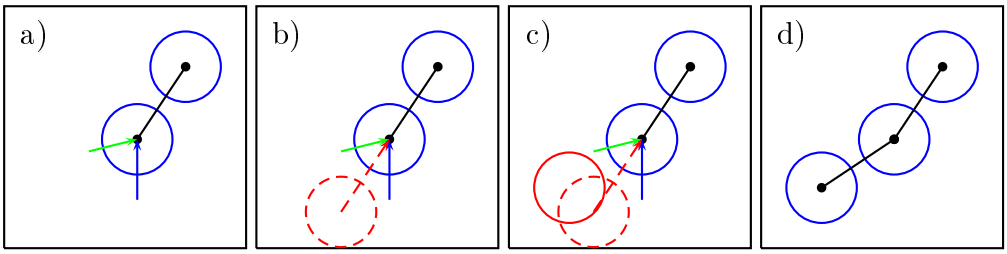

Figure 4.6: Steps of backward tracking: a) two components of the displacement, b) predicting the droplet into the past, c) matching the droplet to the previous image, d) enlarged trajectory

is neglected. Getting some collision rates out of these two dimensional images seems impossible. Figure 4.7 shows the number of trajectories of each file index as well as the number of trajectories which have been enlarged by adding a droplet at the beginning or by fusion of two trajectories.

In figure 4.8 the droplets of the backward tracking are shown with their trajectories as identified in the previous ten frames.

4.3.5 Sort out Unphysical Trajectories

We have now trajectories of droplets which have a minimum length. But looking at videos of the tracked droplets it seems that the preprocessing has not removed all dirt and some is also tracked through the image series. To get rid of these cases, we sort out all trajectories containing droplets which do not move. For each trajectory the maximum distance to the starting point (x_0, y_0) is calculated.

$$d = \max_i \left(\sqrt{(x_i - x_0)^2 + (y_i - y_0)^2} \right) \tag{4.4}$$

x_i and y_i denote the other droplet positions in the trajectory. This distance d is compared to the length of a trajectory of droplet, which is only advected by the fluid (tracer particle). This length is a typical root mean squared velocity $\bar{u}_{rms}$ of the flow times the duration Δt of the trajectory:

$$d_{min} = \frac{1}{2} \bar{u}_{rms} \Delta t \tag{4.5}$$

The factor $1/2$ is there to make the criterion not that sharp. We use $\bar{u}_{rms} = 3\mu\text{m/s}$. All trajectories with $d < d_{min}$ are considered as dirt or droplets sitting on the wall of the measurement cell and deleted.

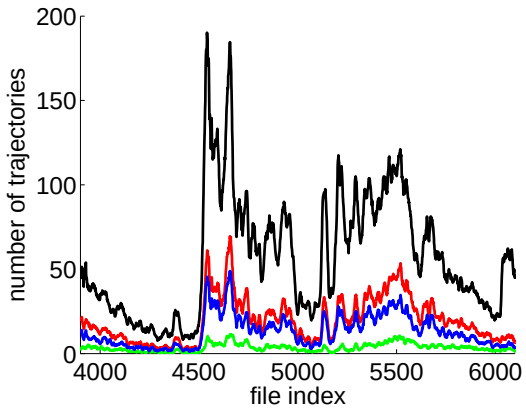

Figure 4.7: Effect of back tracking, the number of trajectories is given per file index: number of all trajectories from forward tracking (black), number of trajectories where at the beginning a droplet has been matched to the image(red), number of trajectories which have been enlarged by one droplet (blue), number of trajectories which have been fused with another trajectory (green). Measurement in the bottom phase, $\xi = 1.05 \cdot 10^{-5}\mathrm{s}^{-1}$, the range of file indices correspond to $\tau = 0.195 - 0.305$.

4.4 Evaluation of the Droplet Tracking Algorithm

4.4.1 Sedimentation Velocities

Figure 4.4 indicates that the small droplets in the system are good tracers for the fluid motion. For the big droplets sedimentation has a significant contribution to the motion. In the implementation of the algorithm the Stokes velocity is assumed to be equal to the sedimentation velocity (equation 4.2). Because we do not have hard spheres sedimenting in a resting fluid but fluid-fluid settling velocities we have to check the agreement with the stokes velocity.

In figure 4.9 the vertical velocity calculated from the trajectories of the tracked droplets is shown as a function of the radius (red data points). The errorbars contains the uncertainties in the radius (see chapter 4.4.4) and the change of the material parameters in the range of averaging. This vertical velocity is compared to the sedimentation velocity due to equation 4.2 (blue points). The mean vertical velocity of the flow (calculated from the flow fields) is added to this velocity. The errorbars of the sedimentation velocity are due to the change of the material parameter in the time interval of averaging. At $r = 0$ the value of the mean flow velocity is plotted, the errorbar of that point denotes the standard deviation of the vertical velocities, which characterises the advection of the fluid.

The assumption of the Stokes velocity seems to describe the vertical component of

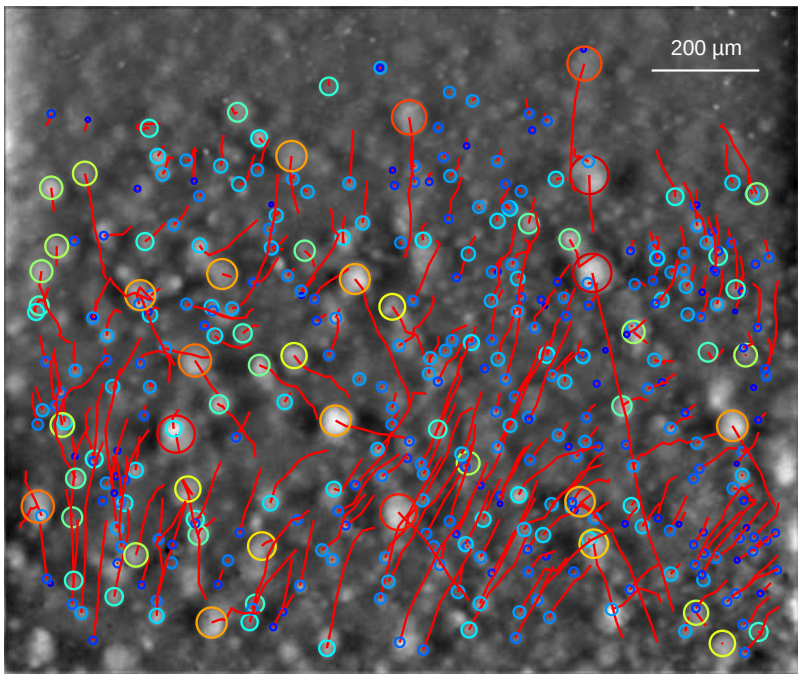

Figure 4.8: All droplets in the image, which are part of a trajectory, are shown. The radius of the droplets is colour coded. The red lines indicate the droplets positions in the last up to ten frames. Measurement in the bottom phase, $\xi = 1.05 \cdot 10^{-5}\mathrm{s}^{-1}$, $\tau = 0.1734$.

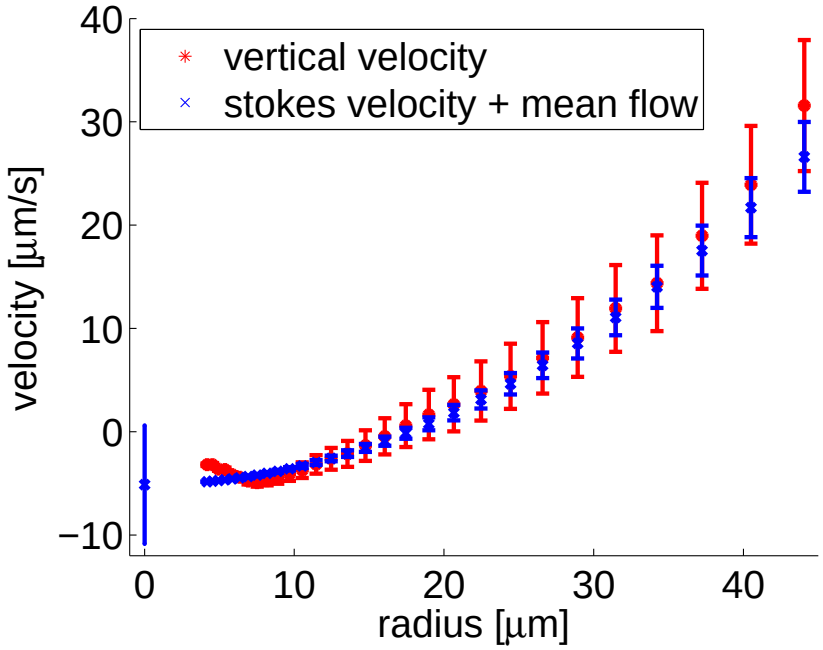

Figure 4.9: Comparision of the vertical velocity of the droplets (red) and the Stokes velocity modified by the mean flow (blue). The data point at $r = 0$ is the mean vertical velocity and the errorbar is the standard deviation, which characterises the variation of the velocity due to the advection.

the velocity very well. For small droplet radii there is a deviation. This is probably due to remaining artefacts. The deviation was much bigger before the unphysical trajectories (see section 4.3.5) were sorted out.

4.4.2 Droplet Numbers

With this algorithm the individual droplets in the images can be tracked through a series of images. This can be visualized very well in a video.
The number of droplets, which are part of a trajectory with a minimum length of three frames, is about 30 to 50% of the number of droplets in the droplet lists. In figure 4.10 the number of droplets is shown as a function of the dimensionless time τ. In this figure it can be seen, that tracking does a tremendous job in reducing the noise. Artefacts of the analysis of single images are sorted out, because they do not have physical trajectories. The backward tracking has not a big effect on the numbers, but it is useful to fill holes in the trajectories and therefore to enlarge them.

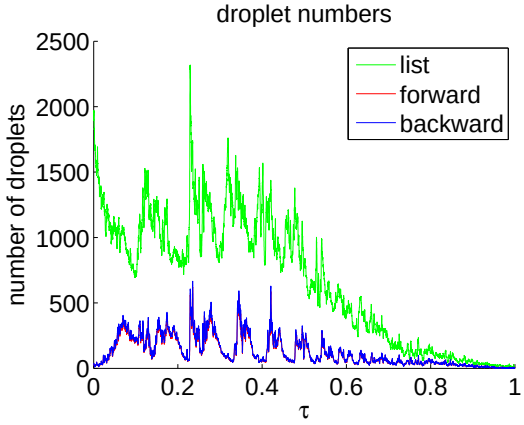

Figure 4.10: Number of droplets: in the droplet list (green), after the forward tracking (red) and after the backward tracking (blue).

4.4.3 Trajectory Length

Small droplets can not be tracked as long as the big droplets. They have to be exactly in the focal plane of the camera to be detectable. For a quantitave analysis trajectories of 2000 images are sorted into radius bins according to their average radius. In each bin the number of trajectories of a given length is colour coded. Figure 4.11 shows the radius dependence of the trajectory length. The red line indicates the time which a droplet of a certain radius needs to sediment through the image due to the Stokes velocity (equation 4.2). It puts an upper bound on the

trajectory length and leads to a decrease of the trajectory length for big radii. For

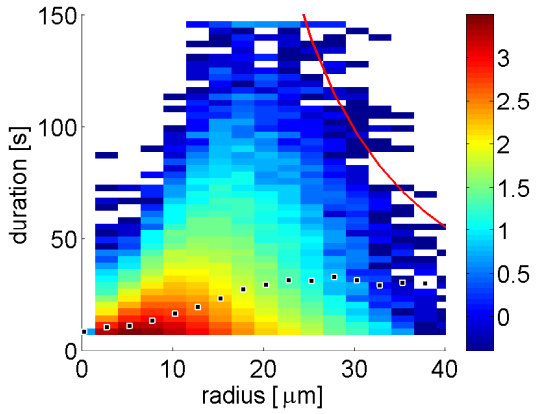

Figure 4.11: Radius dependence of the trajectory length: The number of trajectories with a given radius and length are colour coded on a logarithmic scale. The black squares denotes the average length for each radius bin and the red line is the sedimentation boundary.

small droplets, the trajectory length seems to grow linearly with the radius. We assume that the depth, in which a droplet can be detected, is proportional to its radius. For this measurement 10 seconds correspond to three frames, which is the minimum length of the trajectories.

4.4.4 Estimate the Error of the Radius

To estimate the error of the radius of the detected droplets the radius fluctuations of a tracked droplet along its trajectory can be used. These fluctuations give an estimate of the uncertainty of the radius. The following procedure is used: the average radius is calculated for each trajectory and all the different radius values of one trajectory are put in the one radius bin corresponding to the average radius. At the end the standard deviation of all radius values of one bin is calculated. The result is shown in figure 4.12. Here 100 linear radius bins are used between the radius of 4 and 60μm and the trajectories of the first 10000 images are taken. In the first part up to 19μm a linear increase of the standard deviation is observed, so that there is a constant relative uncertaincy of about 20%. A linear fit gives $\sigma(r) = 0.20 \cdot r - 0.03\mu$m. Above 19$\mu$m the standard deviation is more or less constant and fluctuates because of a small number of big droplets. Here the mean of the values is 3.84μm.

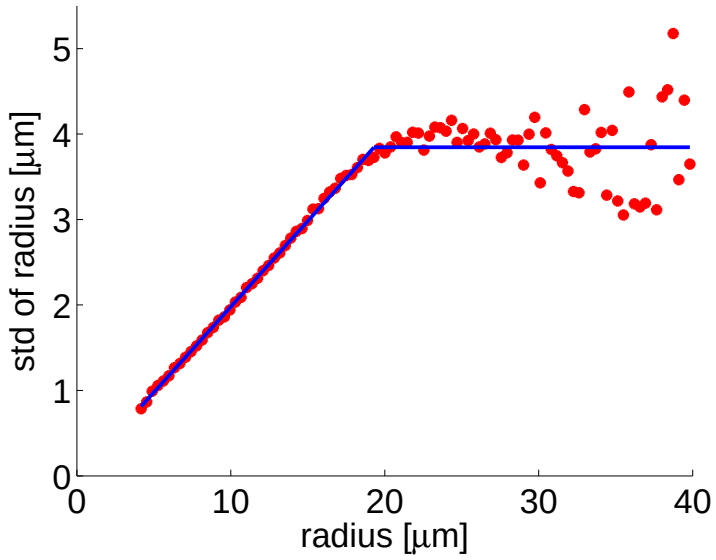

Figure 4.12: Radius-dependent standard deviation of the radius of tracked droplets.

4.5 Summary

In this chapter the established algorithm is described, which can detect and track the droplets through an image series. Additionally to the position the radius of the droplets is used for the tracking. The sedimentation of the droplets, described very well by the Stokes velocity, is taken into account explicitly. With this tracking algorithm we have access to the trajectories of the droplets and the velocity field of the fluid. From the trajectories of the droplets the size distribution can be calculated, because they contain also the radius information. This will be done in the next chapter together with the characterization of the flow field.

5 Characterizing Droplet Size Distribution and Flow Field

5.1 Size Distribution

The outcome of the analysis of the images are trajectories of the droplets. First of all we are interested in the size distribution of droplets: how many droplets of a given radius are in the system at a given time. To get the size distribution out of the trajectories the following procedure is done. First the droplets of each image are sorted into logarithmic radius bins according to their radius. The numbers in the radius histogram are divided by the bin width, to get a number which is independent of the bin size (this is important, because logarithmic radius bins are used). Afterwards the time binning is made by averaging the data in each time bin.
To get a number density the number of droplets has to be divided by the sample volume, in which the droplets are detected. Because the images are two dimensional the sample area is defined as the area in which the droplets are taken into account. For the depth it is not so clear which length should be considered. It seems that in the experiment the probability of detecting a droplet is proportional to its radius. The analysis of the trajectory length show that the average trajectory length increases with the radius (see figure 4.11). The calibration of the radius dependent probability of the droplet detection has to be done more precisely. In this work the assumption is used that the depth where a droplet can be detectedis twice the diameter of the droplet[1]. Dividing the number of droplets by the radius dependent depth of field and by the sample area gives the number of droplets per volume.
A part of the size distribution is shown as a 3d plot in figure 5.1. The height corresponds to the number density. We see clear oscillations in the size distributions. Now we have access to the full distribution of droplet sizes. In the turbidity measurements only one moment of the size distribution can be measured.
In the following, the size distributions are presented in two dimensional plots, where the droplet number density is colour coded to make comparisons between distributions easier and have a better view of the whole distribution.
A way of checking the assumption of the radius-dependent probability of the droplet detection is to look at the droplet volume fraction. With the number density $n(r)$

[1] There is a good argument using the oscillations of the size distribution to show that this assumption works. Because we first want to calculate the size distribution, this is given later.

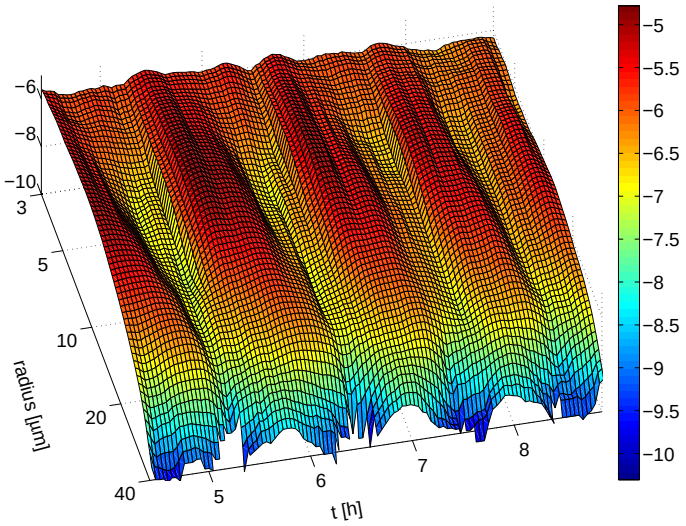

Figure 5.1: Droplet number density as a function of time and radius: the intermediate part of a measurement in the bottom phase with $\xi = 1.05 \cdot 10^{-5}\mathrm{s}^{-1}$ is shown. The decadic logarithm of the droplet number density is colour coded.

the droplet volume fraction v can be obtained by integration:

$$v = \int \mathrm{d}r n(r) \frac{4\pi}{3} r^3 \tag{5.1}$$

This droplet volume can be compared to the generated droplet volume by heating the system (see equation **??**). Since ξ is kept constant the generated droplet volume fraction in a certain time t is given by $v = \xi \cdot t$.

In figure 5.2 the change in droplet volume fraction Δv_{sd} between each minimum and maximum of an oscillation is compared to the generation of droplet volume due to $\Delta v_\xi = \xi \cdot t$, where t is the time between the minimum and maximum of an oscillation. Of course there are deviations but in principle the assumption seems to be justified.

5.1.1 Comparison of the Size Distribution Before and After Droplet Tracking

It is also possible to calculate the size distribution from droplets lists resulting from the image processingof single images. This is done to point out the importance of the droplet tracking in the process of data analysis. Comparing the two size

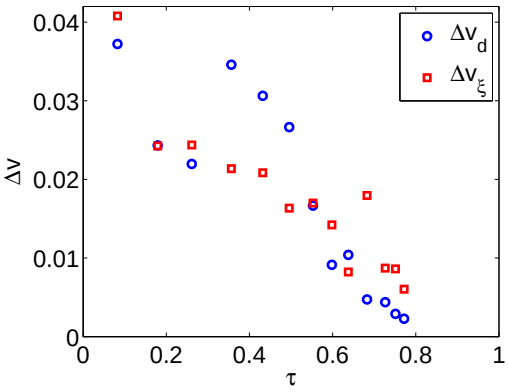

Figure 5.2: Comparison of the droplet volume fraction created between the minimum and maximum of each oscillation (bottom phase with $\xi = 1.05 \cdot 10^{-5}\mathrm{s}^{-1}$). Δv_{sd} denotes the change in measured droplet volume fraction and Δv_ξ the expected change in droplet volume fraction due to the driving of the system.

distributions in figure 5.3, the effect of the droplet tracking is clearly visible. For the small droplets the noise is reduced significantly and some structure of the size distribution can also be seen here. The effect of the droplet tracking is also visible in the droplet number density (see figure 5.4), where it removes a backround mainly appearing in the first half of the measurement. The oscillations are visible more clearly.

5.1.2 Evolution of the Size Distribution during the Oscillation

To see how the droplet volume is distributed during the oscillations and to see how the droplets grow we plot the volume density of the droplets. The volume density per radius $V(r)$ is related to the number density $n(r)$: $V(r) = n(r) \cdot \frac{4\pi}{3} r^3$. For the analysis the oscillations four, five and six are taken. They are divided into 12 parts. For the start and end time of the oscillation the average time of the minimum in the number density and the droplet volume fraction is taken. If both moments of the size distribution are considered for the determination of the start and end points of the oscillations, the result is more robust. For each part the volume density is averaged in time. In figure 5.5 the volume densities for the three oscillations are shown. The 12 different parts are colour coded. At the onset of the oscillation the volume is mainly given by the volume of big droplets remaining from the last oscillation. In part three and four the small droplets start to contribute a considerable amount of volume. A peak of droplet volume is formed at small radii. The droplets grow and therefore the peak shifts to higher radii. In the last third of the oscillation the peak decreases in height, because the droplets sediment and droplet volume is transported

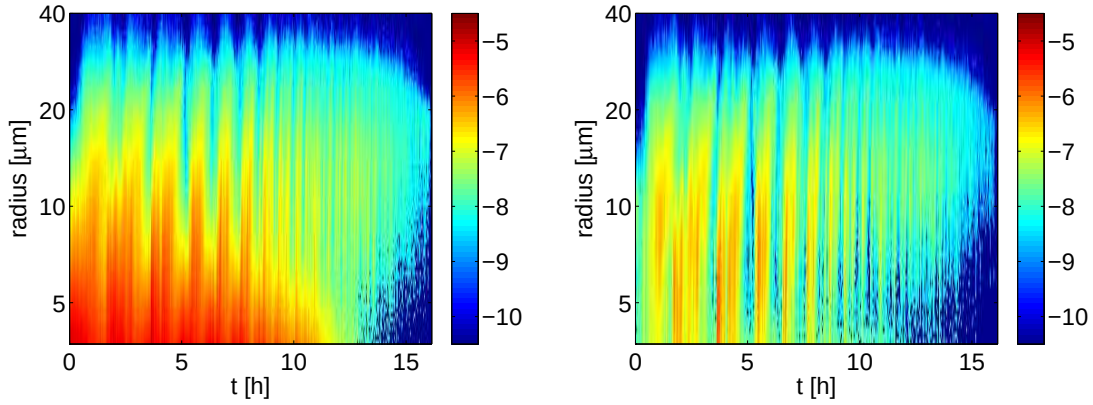

Figure 5.3: Size distribution of droplets of the bottom phase with $\xi = 1.05 \cdot 10^{-5}\mathrm{s}^{-1}$: before the tracking (left) and after the tracking (right). The droplet number density per radius given in $\mu\mathrm{m}^{-4}$ is colour coded on a logarithmic scale.

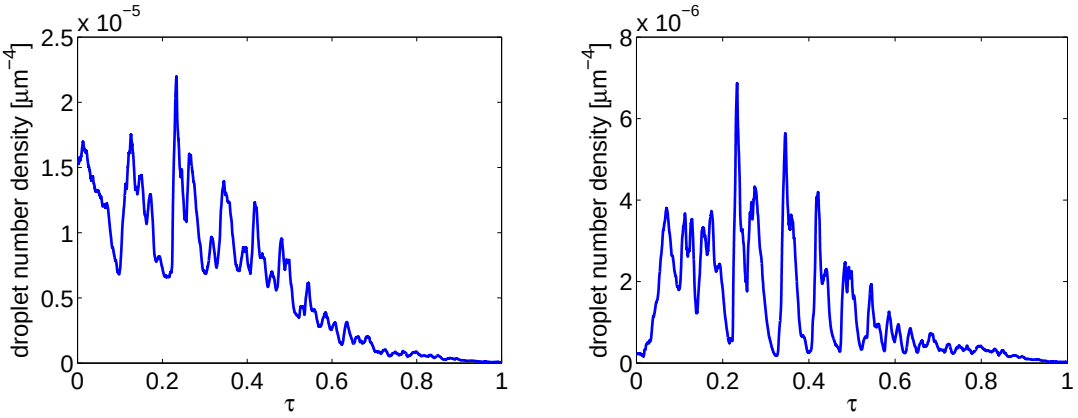

Figure 5.4: Droplet number density of the bottom phase with $\xi = 1.05 \cdot 10^{-5}\mathrm{s}^{-1}$: before the tracking (left) and and after the tracking (right).

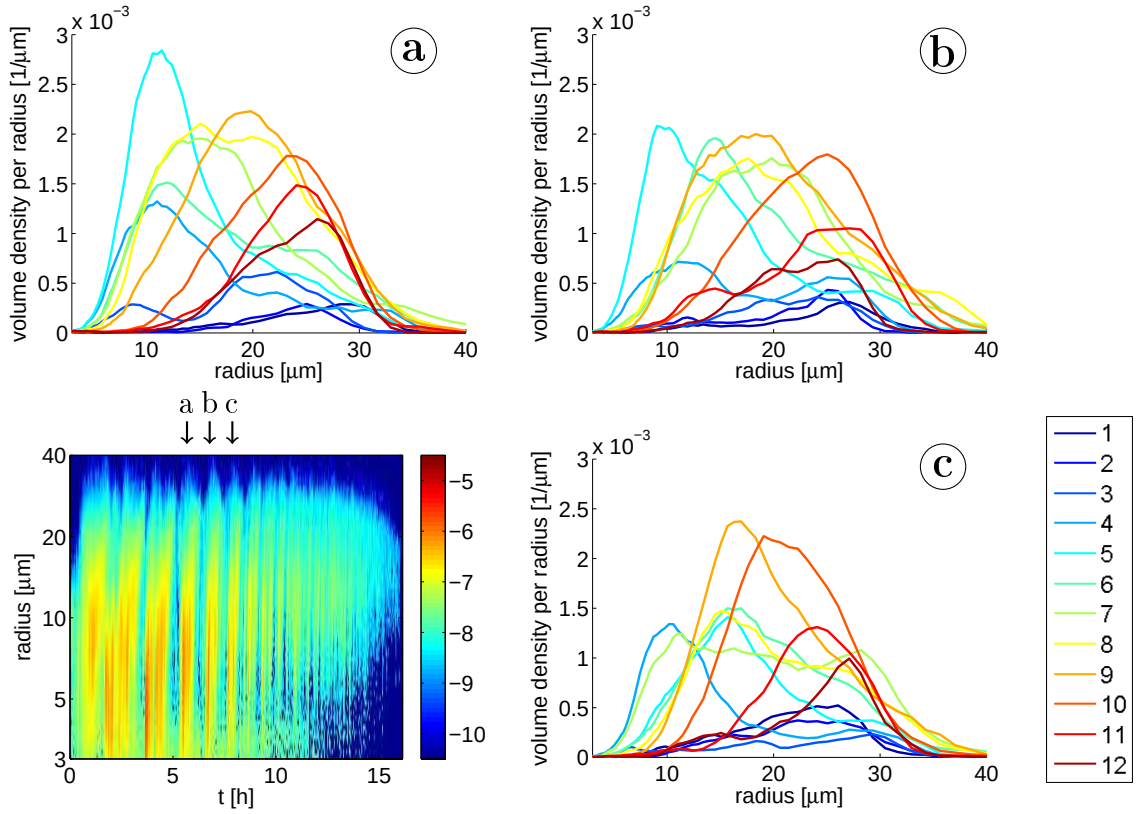

Figure 5.5: Evolution of the size distribution: number density of the whole measurement of the bottom phase with $\xi = 1.05 \cdot 10^{-5}\mathrm{s}^{-1}$ (lower left). In the other three figures the droplet volume density is shown for the 12 parts of each oscillation. a,b, and c correspond to the fourth, fifth and sixth oscillation in the size distribution.

to the interface.
At the beginning of an oscillation, when the new droplets are generated, there is still a considerable amount of big droplets in the system. In this part the distribution becomes bimodal. This has been also observed in droplet size distributions of clouds. cite
A possible explanation for the remaining big droplets is, that they are nucleated at the bottom of the measurement cell and drop off when they have reached a certain size.
The area underneath the lines corresponds to the volume fraction at that time (it is the radius integral of the volume density per radius). For the first half it increases due to the droplet growth. Then the droplet volume fraction decreases, because the droplets sediment.

5.2 Characterization of the Flow Field

If the flow is affected by the sedimenting droplets in the system this should result in density driven advective flow patterns. Spatial and temporal correlations of the flow field can characterise the duration and the size of these random structures. This will be analysed in the first part.
The fluid motion has to compensate somehow the mass flux of the sedimenting droplets. We have seen that the size distribution shows oscillations. These oscillations should therefore also appear in the the flow field. This will be addressed in the second part.
The displacement fields resulting from of the droplet tracking procedure can be easily converted into velocity fields of the fluid by multiplying them with the framerate of the image series.

5.2.1 Spatiotemporal Correlations

The velocity field consits of m x n discrete velocities, m in the vertical (x) and n in the horizontal (x) direction. The mean velocity $\bar{u}_x(t)$ of the velocity field $u_x(i,j,t)$ is given by:

$$\bar{u}_x(t) = \frac{1}{m \cdot n} \sum_{i=1}^{m} \sum_{j=1}^{n} u_x(i,j,t) \tag{5.2}$$

There are different numbers of droplets in the images, because the size distribution oscillates. Therefore not every point in the velocity field is defined at every time. For the calculation of the mean velocity as well as for the correlation functions the points of the velocity field, which are not defined, are neglected.

5.2.1.1 Correlation Time

The correlation function of two velocity fileds, which are separated by the time Δt is given by:

$$cor_{xx}(\Delta t) = \frac{\sum\sum \left(u_x(i,j,t) - \bar{u}(t)\right) \cdot \left(\left(u_x(i,j,t+\Delta t) - \bar{u}(t+\Delta t)\right)\right.}{\sqrt{\sum\sum \left(u_x(i,j,t) - \bar{u}(t)\right)^2 \cdot \sum\sum \left(u_x(i,j,t+\Delta t) - \bar{u}(t+\Delta t)\right)^2}} \tag{5.3}$$

The correlation function is evaluated for all pairs of Δt in a time interval of the measurement. The averaged correlation function consists of the averages of all values of the same Δt. Figure 5.6 shows the result for a measurement in the bottom phase with $\xi = 1.05 \cdot 10^{-5}\mathrm{s}^{-1}$ for 3000 consecutive velocity fields in the first half of the meausrement.
The correlation function decays exponentially with a correlation time τ:

$$cor(\Delta t) = A \cdot \exp\left(-\frac{\Delta t}{\tau}\right) \tag{5.4}$$

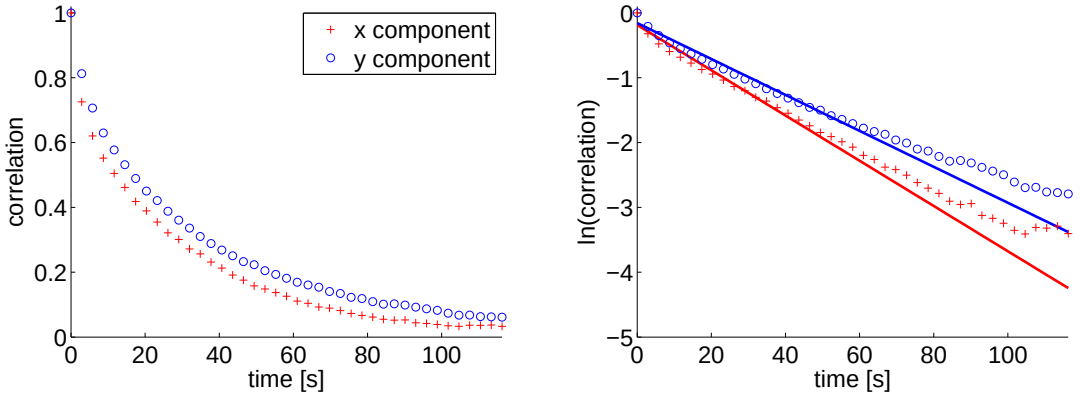

Figure 5.6: Temporal correlation function of the velocity field: horizontal component (red) and vertical component (blue)

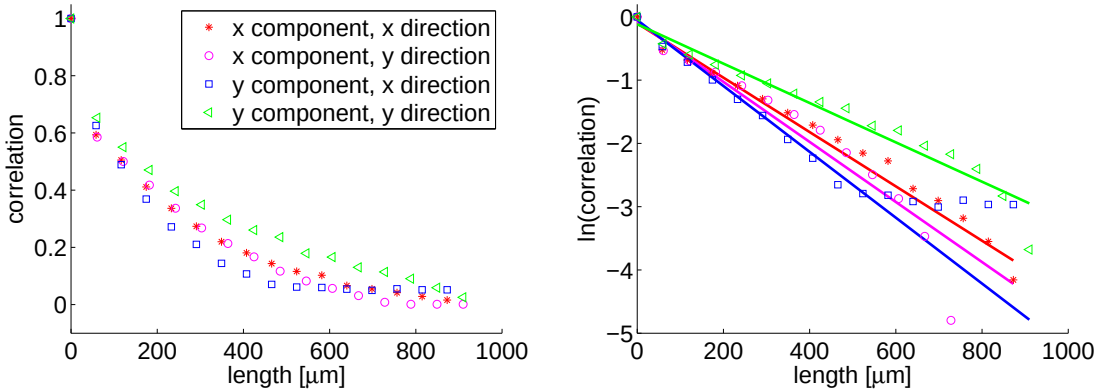

Figure 5.7: Spatial correlation function of the velocity field

For the horizontal components the fitparameters are $A_x = 0.83$ and $\tau_x = 29$s and for the vertical component $A_y = 0.86$ and $\tau_y = 36$s.

5.2.1.2 Correlation Length

For the spatial correlations four different correlations are distinguished. There are two components of the velocity field, which could have different correlations in each direction respectively. For each velocity field the correlation (in this case it is the auto correlation of the velocity field) is calculated. These correlations are averaged over a time interval which is longer than the correlation time. The correlation function is shown in figure 5.7. Here the same data is used as for the calculation of the temporal correlations. Values of the correlation function for larger distances than 900μm can not be calculated, because the image is only 1.3mm x 1.5mm in size.

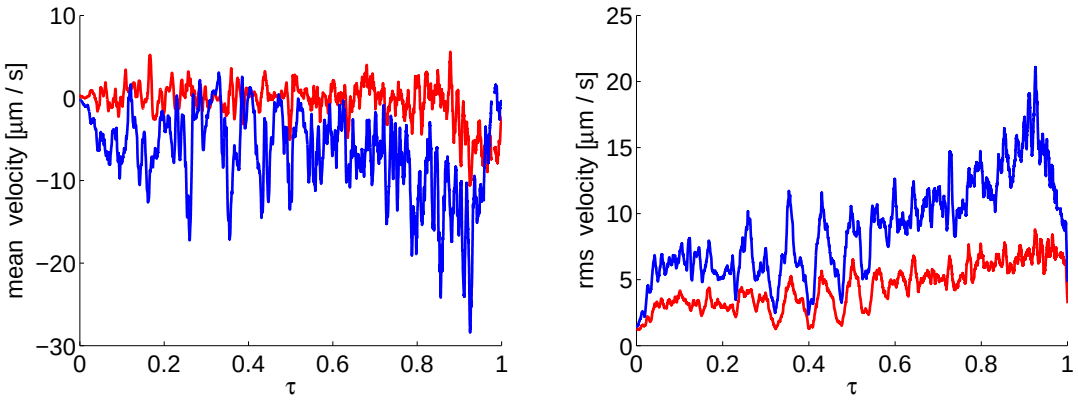

Figure 5.8: Velocities (left) and rms velocities (right) of the fluid, horizontal component (red), vertical component (blue), $\xi = 1.05 \cdot 10^{-5}\mathrm{s}^{-1}$.

The spatial correlations also decay exponentially with a correlation length γ. The correlation length of the vertical component in vertical direction is $\gamma = 321\mu$m and slightly higher than the other three values. They lie between 192μm and 232μm.

5.2.2 Oscillations of the Flow Field

In figure 5.8 the vertical and the horizontal component of the velocity field and the root mean squared velocities are shown as a function of the dimensionless time for a complete measurement. The values are averaged values of all velocity vectors present in one velocity field. The horizontal component fluctuates around zero velocity. This reflects that there is no preference for motion to the left and to the right. After all, measurements are performed near the front wall of the cell, but in the center with respect to the other two walls. For the vertical flow the situation is different – its average value is negative, i.e. the fluid has the tendency to move downwards. There are two possibilities to explain the downward moving of the fluid. First the fluid has to compensate the volume flux of the upward sedimenting droplets and second there are convection cells in the measurement cell. The convection cells in the sample are induced by the heating from outside the measurement cell. That means that the fluid at the wall of the cell is slightly warmer than in the center. The convection cell is at least driven by density differences. The density of the fluid is lower if the temperature is higher, but the binary fluid also demixes. This means that in the bottom phase the water content is increased and therefore the density also (see figure 5.9 (left)). Up to 33°C the demixing effect is dominant and the fluid has a higher density if it is warmer (see figure 3.4(left)). 33°C corresponds to $\tau \approx 0.85$ for ξ_l (see figure 3.11 a)). In the top phase both effects lower the density. This leads to counter rotating convection cells in the top and bottom phase. In the bottom phase

the fluid moves downwards at the wall of the cell and in the top phase upwards (see figure 5.9 (right)).
In the following we consider two parts of the measured vertical fluid velocity $u_f = u_c + u_{bulk}$, where u_c is the convective part due to the convection cell in the measurement cell and u_{bulk} denotes the velocity of the bulk, which compensates the volume flux of the sedimenting droplets.
Now we have a look at the contribution of the droplets. From the size distribution

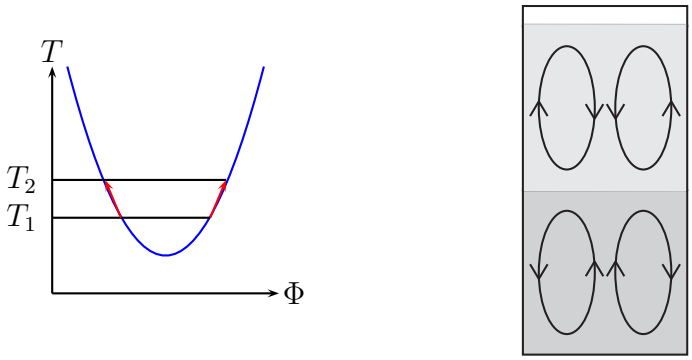

Figure 5.9: Convection cells. Left: phase diagram, for the higher temperature (T_2) the system is demixed further. The bottom phase contains more water compared to T_1 (has a higher density) and the top phase more i-BE (has a lower density). Right: resulting convection cells, shown is a vertical cut through the center of the measurement cell.

a volume averaged sedimentation velocity is calculated. It is the integral over the sedimentation velocity u_{sed} (see equation 4.2), the droplet volume ($\frac{4\pi}{3}r^3$) and the droplet density ($n(r)$), normalized by the droplet volume fraction:

$$u_{dr} = \frac{\int \mathrm{d}r n(r) \frac{2}{9} \frac{\Delta\rho g r^2}{\eta} \frac{4\pi}{3} r^3}{\int \mathrm{d}r n(r) \frac{4\pi}{3} r^3} \tag{5.5}$$

The sedimentation velocity is relative to the velocity of the surrounding fluid.
In figure 5.10(left) the sedimentation velocity u_{dr} and the fluid velocity u_f are shown. The sedimentation velocity increases during the measurement significently, because the density difference $\Delta\rho$ increases and the viscosity decreases (see equation 5.5 and figure 3.4 and 3.5). Both curves show oscillations.
To see the effect of the sedimenting droplets on the bulk velocity, the comparison of the upward and downward moving volume has to be done in a frame comoving with the convection velocity u_c. For this comparison an effective volume fraction v_{hyd} has to be taken into account, because the droplets may not carry only their own volume, but also some surounding fluid. The droplets move upwards with the

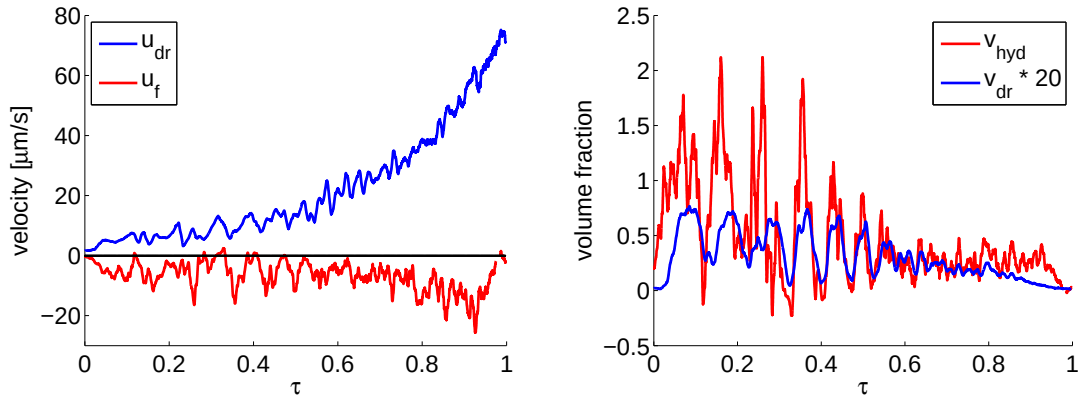

Figure 5.10: Left: velocities of the fluid (red) and the droplets (blue), right: hydrodynamic volume fraction (red) and droplet volume fraction increased by a factor of 20 (blue).

velocity of $u_{dr} + u_{bulk}$. Volume conservation gives:

$$0 = v_{hyd} \cdot (u_{dr} + u_{bulk}) + (1 - v_{hyd}) \cdot u_{bulk} \tag{5.6}$$

This equation gives with $u_f = u_{bulk} + u_c$:

$$v_{hyd} = -\frac{u_f - u_c}{u_{dr}} \tag{5.7}$$

Unfortunately we can only measure u_f and u_{dr}. In the following we assume, that the hydrodynamic volume fraction v_{hyd} is proportional to the droplet volume fraction v ($v_{hyd} = C \cdot v$). Since we have two unknowns, we can discuss only the two limiting cases. One is a small convection velocity, which can be neglected compared to the fluid velocity, and the other is $C = 1$ where the droplets only carry their own volume. First we neglect the convection velocity. In figure 5.10(right) $v_{hyd} = -\frac{u_f}{u_{dr}}$ is given for a complete measurement. The hydrodynamic volume fraction fits very well to the oscillations of the droplet volume fraction in the middle of the measurement. In the end the uncertainties in the velocity field are bigger, because only a few droplets exist in each image. The droplet volume fraction is multiplied by a factor of about 20 to get this agreement with the hydrodynamic volume fraction. This means if the convective flow is neglegeble, the hydrodynamic radius of the droplets, where they effect the surrounding fluid, is by a factor of $\sqrt[3]{10} \approx 2.7$ bigger than the droplet radius.
But there is a big problem in this limiting case. The hydrodynamic volume fraction reaches unphysical values. A volume fraction is per definition equal or smaller than 1 (in figure 5.10(right) it goes up to 2). This means that only the effect of the sedimenting droplets cannot explain the velocity of the flow. To get resonable

values of v_{hyd} the convective velocity has to have a significient contribution. It lowers the modulus of the numerator in equation 5.7 (u_f and u_c are both negative in the bottom phase).
In the other limiting case where the droplets only carry their own volume ($C = 1$), we can estimate the relation of the measured fluid velocity u_f and the convective velocity u_c. In figure 5.10(left) in the middle of the measurement the sedimentation velocity u_{dr} and the fluid velocity u_f have values of about 10 μm/s (but in opposite directions). From equation 5.7 we get with $u_f \approx -u_{dr}$ and $v_{hyd} = v$:

$$\frac{u_c}{u_f} = 1 - v = 0.98 \text{ to } 0.96 \tag{5.8}$$

because the volume fraction has values between 2 and 4%. In this limiting case the sedimenting droplets hardly influence the fluid velocity.
The vertical component of the velocity field can be qualitatively explained by the downward flow of a convection cell and a oscillatory volume flux compensation of the sedimenting droplets by the flow. With our experimental data it is not possible to give a quantitative discussion.

5.2.3 Distribution of Velocities

The previous part shows the connection between the oscillations in the size distribution and the flow field. To have a closer look how the oscillations evolve in the flow field during an oscillation, we will analyse the distribution of the velocities in the velocity field. Each oscillation is divided into four time intervals of equal length according to the oscillations in the number density (or the volume fraction). The first one is centered around the minimum and the third one around the maximum of the number density and the other two parts are located in the region where the number density rises or decreases. For each part of the oscillation the cumulative distribution of the horizontal and vertical component is calculated from the velocity fields. In figure 5.11 an averaged cumulative distribution is shown. The distribution of the horizontal component is centered around zero velocity as expected and is fairly symmetric. The width is changing a little from part to part of the oscillation. The distribution of the vertical velocity is shifted to negative velocities, so there is a mean velocity of the fluid pointing downwards. Until reaching part three of the oscillation the distribution is getting broader and shifts to the left.
In figure 5.12 the mean of each part of the oscillation is shown for all oscillations apparent in the measurement. The errorbars correspond the the standard deviation of the distribution divided by the square root of the number of uncorrelated velocities. This number can be calculated using the correlation time and length. After the doubled correlation time (about one minute) the velocity fields are assumed to be uncorrelated, so one velocity can be used every minute. The correlation length is about 300μm, assuming again the doubled value for the vanishing correlation there

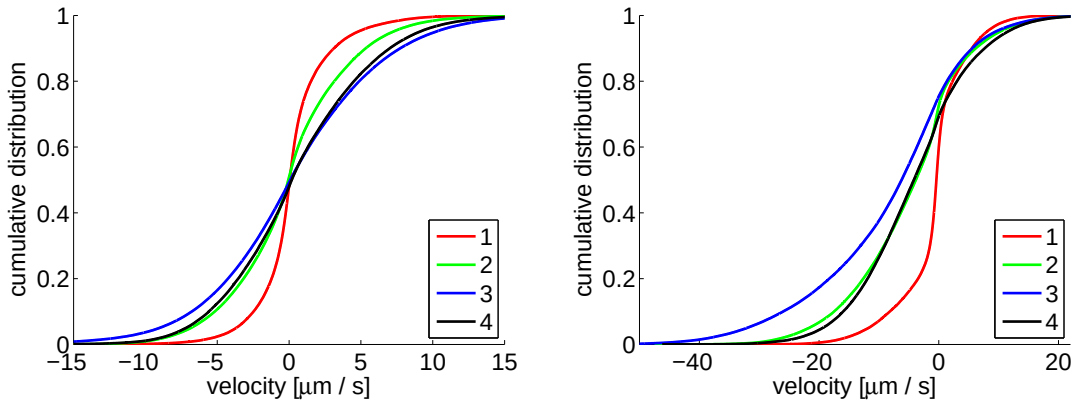

Figure 5.11: Cumulative distribution of the horizontal (left) and vertical component (right) of the velocity field. It refers to a measurement in the bottom phase, $\xi = 1.05 \cdot 10^{-5}\mathrm{s}^{-1}$, averaged over oscillations 3 - 6.

are about four uncorrelated parts of each velocity field (image is about 1.3mm x 1.5mm). In figure 5.12 the root mean squared velocities are shown for each part of the oscillations (dashed lines). Like the mean velocities they also show oscillations. In the middle of one oscillation the vertical component has a minimum and the root mean squared velocity has a maximum. The oscillation period decreases and the errorbars at least for the mean velocities increase because of fewer data points. In figure 5.13 the corresponding size distributions are shown. The oscillations are also divided in four parts as above.

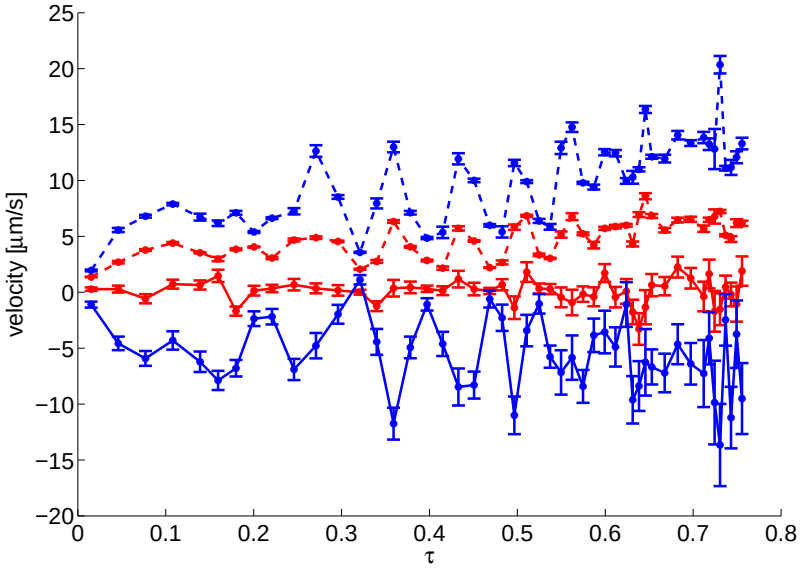

Figure 5.12: Mean velocity in horizontal (red) and vertical (blue) direction (solid line), rms velocity (dashed line) in horizontal (red) and horizontal (blue) direction. For all 12 oscillations, four consecutive data points correspond to one oscillation. Measurement in the bottom phase, $\xi = 1.05 \cdot 10^{-5}\mathrm{s}^{-1}$.

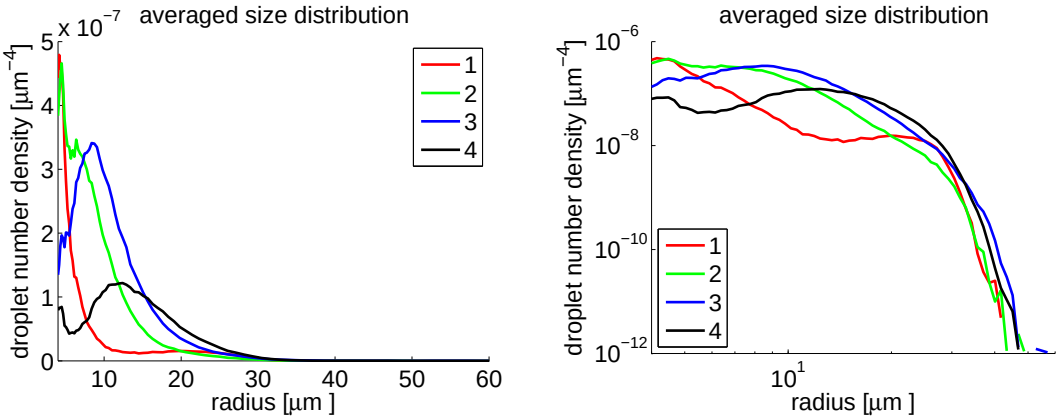

Figure 5.13: Number density of the four parts of the oscillations for the bottom phase and $\xi = 1.05 \cdot 10^{-5}\mathrm{s}^{-1}$. Average over the oscillation 3-6. On the right hand side the number density is shown on a log-log-scale.

6 Conclusions

6.1 Discussion

With the experimental setup we are able to take images of droplets in binary phase separation, in a plane near the wall of the measurement cell. To look much deeper than 300 μm (about one and a half of the correlation length of the flow field) into the fluid is not possible. The droplet-rich system is comparable to dense fog with limited sight.
From the measured phase boundaries of the binary system we are able to design temperature ramps, which are adapted to the phase diagram. Temperature ramps with a constant thermodynamic driving have already been used in experiments by [10], but in a way that the mass flux between the two phases is kept constant. In our case we adapt the driving force to the situation in the bottom or top phase, which leads to physical interpretation of the driving force as the generated droplet volume per unit time.
With the established droplet tracking algorithm we are able to get the size distribution of the droplets as well as the droplet velocities and the velocity of the flow simultaneously. The widely used particle tracking velocimetry (PTV) [25–27] uses monodisperse tracer particles. The positions of the particles in the images have to be detected with image processing. Tracking of the identified particles in 3D leads to trajectories. These particle tracking algorithms can not be adapted to our system, because additional tracer particles will alter the system. They may act as nucleation sites and stick to the interface between droplets and bulk and influence the growth rate [28] and the coalescence of droplets [29, 30]. We use the droplets present in the system to get information of the flow. The radii of the detected droplets cover a range of 4μm to 40μm and some are even larger, but very rare. Therefore the tracking algorithm has to deal with a polydisperse system. Additionally to the position the radius of the droplets is taken into account. On the one hand, the radius is an additional criterion to identify one physical droplet in a sequence of images. On the other hand, the movement of the droplets has to be decomposed into advection and sedimentation, since the densities of droplets and bulk are not matched. The Stokes velocity describes the sedimentation of the droplets very well (see figure 4.9). The advective component of the displacement is used for the calculation of an advective flow field. With the tracking of the droplets artefacts in the detection of the droplets are eliminated, this results in noise reduction of the size distribution especially for

small droplets.
The droplet tracking algorithm is used in our experiment for a low Reynolds number flow. But it can also be used for turbulent flow, if the framerate of the camera is adapted to the velocity of the droplets.
The measured size distributions show clear oscillations. The oscillations have been observed before only by measurements of turbidity and heat capacity [9, 10, 12].With the size distribution we additionally can see how the droplet volume is distributed during the oscillations.
In the size distribution we observe sometimes a bimodal size distribution of droplets. This has been reported also for clouds. cite lamb
The flow field has been characterized by spatiotemporal correlations and by the time-dependent mean flow and the root mean squared velocity of the flow. The size of the advective flow patterns have been calculated from the correlation length. The flow patterns extend 200 - 300μm in space and have a life time of about 30s at least for the measurement of $\xi = 1.05 \cdot 10^{-5}\mathrm{s}^{-1}$ in the bottom phase. The mean vertical velocity and the root mean squared velocity show oscillations. Qualitatively they can be linked to the oscillations in the size distribution.

6.2 Outlook

At the end of my thesis there are of course open questions, possibilities for additional experiments and optimisation of the droplet tracking.
The vertical component of the flow field can only be explained qualitatively by the flow of a convection cell and the compensation of the volume flux of the sedimenting droplets. With a change of the sample geometry, e.g. change in the aspect ratio, the convection cell should be affected, whereas the compensation of the volume flux should stay the same. With these additional experiments the two effects can hopefully be seperated.
With the magnetic stirrer we have the possibility to mix the sample from the bottom of the measurement cell. Test measurements with a slight mixing (50 rounds per minute) show a break down of the oscillations in the bottom phase. With the externally disturbed flow maybe the influence of the flow field on the oscillations can be studied. A reactive–flow model of phase separation [31] shows that the oscillation periods are hardly affected by the flow.
With our experimental setup we can only measure near the wall of the measurement cell. With an endoscope technique [32] images can be taken intrusively also from inside the measurement cell.
In the droplet tracking algorithm a discrete displacement field is used for the prediction. It does not matter where in the cell of the displacement field the droplet is located. Here the prediction can be optimized, if an interpolation between the cell of the droplet and the neighbouring cells is used.

A detailed analysis of the oscillation periods is current work of Tobias Lapp. The oscillation periods depend on the heating rate and on the material parameters of the system. To verify the dependence on the material parameters, it would be nice to investigate another binary liquid, e.g. the methanol-hexane system. It has already been studied by turbidity and heat capacity measurements [10].
The droplet growth during the oscillatory phase separation of the binary fluid can be modelled (current work of Michael Wilkinson, Jürgen Vollmer and Tobias Lapp) by two meachanisms: the droplet growth due to the theory of Ostwald ripening and a finate-time runaway growth, where large droplets sweep up smaller ones. This thesis contributes to the experiments, which are in good agreement with this model. This model will be published soon.

Appendix

1 Conversion between Different Composition Units

There are three common units for the composition: mass fraction Φ^m, volume fraction Φ^V and molar fraction Φ^n. In the literature all of them are used. So here conversion formulars are given.
The different fractions (for compound 1) are defined as follows:

$$\Phi_1^m = \frac{m_1}{m_1 + m_2} \tag{1}$$

$$\Phi_1^V = \frac{V_1}{V_1 + V_2} \tag{2}$$

$$\Phi_1^n = \frac{n_1}{n_1 + n_2} \tag{3}$$

To convert these fractions the desities ρ_1, ρ_2 and the molar masses M_1, M_2 of the two compounds are needed. Substituting with the relation $m = \rho \cdot V$ and $m = n \cdot M$ leads to the following conversion formulas:

$$\Phi_1^m = \frac{1}{1 + \frac{\rho_2}{\rho_1}\left(\frac{1}{\Phi_1^V} - 1\right)} \qquad \Phi_1^V = \frac{1}{1 + \frac{\rho_1}{\rho_2}\left(\frac{1}{\Phi_1^m} - 1\right)} \tag{4}$$

$$\Phi_1^V = \frac{1}{1 + \frac{M_2\rho_1}{M_1\rho_2}\left(\frac{1}{\Phi_1^n} - 1\right)} \qquad \Phi_1^n = \frac{1}{1 + \frac{M_1\rho_2}{M_2\rho_1}\left(\frac{1}{\Phi_1^V} - 1\right)} \tag{5}$$

$$\Phi_1^n = \frac{1}{1 + \frac{M_1}{M_2}\left(\frac{1}{\Phi_1^m} - 1\right)} \qquad \Phi_1^m = \frac{1}{1 + \frac{M_2}{M_1}\left(\frac{1}{\Phi_1^n} - 1\right)} \tag{6}$$

2 Calculation of the Densities for Different Compositions

For the calculations of the densities for the two phases of the system i-BE / water the data of [21] is used. There are two effects which change the density. In real systems it is often the case that the volume of the two mixed components is smaller than the sum of the volume before mixing, that the system has a negative excess

volume V_E. On the other hand the density depends on the temperature. For this case a simple formula depending on the volume fraction can be derived. Starting point is the definition of the density:

$$\rho = \frac{m}{V} = \frac{m_{H_2O} + m_{iBE}}{V} = \frac{\rho_{H_2O} V_{H_2O} + \rho_{iBE} V_{iBE}}{V} = \rho_{H_2O}(1 - \Phi^V) + \rho_{iBE}\Phi^V \quad (7)$$

where $V = V_{H_2O} + V_{iBE}$ and $\Phi^V = V_{iBE}/V$ (see equation 2). For the densities the values measured in [21] are used. They give values for a linear approximation of the densities:

$$\rho(T) = \rho(T = 25°C) - \alpha \cdot T \quad (8)$$

The values are given in table 1.

If the excess volume V_E is also regarded, the formulas become more involved. The

	i-BE	water
$\rho(25°C)/(g \cdot cm^{-3})$	0.886255	0.997043
$\alpha/(1000K^{-1})$	0.968	0.2571

Table 1: Densities and thermal expansion coefficients for water and i-BE, taken from [21]

excess volume has to be added to the ideal volume in the previous case:

$$\rho = \frac{m}{V_{ideal} + n \cdot V_E^n} = \frac{m_{H_2O} + m_{iBE}}{V_{ideal} + n \cdot V_E^n} = \frac{m_{H_2O} + m_{iBE}}{\frac{m_{H_2O}}{\rho_{H_2O}} + \frac{m_{iBE}}{\rho_{iBE}} + n \cdot V_E^n} \quad (9)$$

n is the sum of the moles of the two components: $n = m_{H_2O}/M_{H_2O} + m_{iBE}/M_{iBE}$. Now the mass of each component can be converted into mass fractions of i-BE (Φ^m):

$$\rho = \frac{1}{\frac{1-\Phi^m}{\rho_{H_2O}} + \frac{\Phi^m}{\rho_{iBE}} + \left(\frac{1-\Phi^m}{M_{H_2O}} + \frac{\Phi^m}{M_{iBE}}\right) \cdot V_E^n} \quad (10)$$

The molar excess volume V_E^n itself is also a function of the composition (in molar fraction Φ^n). This data is also taken from [21]. For 25°C they provide a formula to get V_E^n for each composition Φ^n:

$$V_E^n(\Phi^n) = \frac{\Phi^n(1 - \Phi^n)}{1 - G(1 - 2\Phi^n)} \cdot (A_1 + A_2(1 - 2\Phi^n) + A_3(1 - 2\Phi^n)^2) \quad (11)$$

The parameters are fit parameters to their data: $G = 0.975$, $A_1 = -3.079 cm^3/mol$, $A_2 = 1.801 cm^3/mol$ and $A_3 = 0.839 cm^3/mol$. The composition in mass fraction can be converted into a composition in molar fraction with equation 6 to use this fit function. In this case the temperature dependence of the excess volume is neglected.

Bibliography

[1] R. A. Shaw, "Particle-turbulence interactions in atmospheric clouds," *Annual Review of Fluid Mechanics*, vol. 35, no. 1, pp. 183–227, 2003.

[2] R. Pachauri and A. Reisinger, *IPCC, 2007: Climate Change 2007: Synthesis Report. Contribution of Working Groups I, II and III to the Fourth Assessment Report of the Intergovernmental Panel on Climate Change*. Intergovernmental Panel on Climate Change, 2008.

[3] K. Beard and H. Ochs, "Warm-rain initiation: An overview of microphysical mechanisms," *Journal of Applied Meteorology and Climatology*, vol. 32, pp. 608–625, April 1993.

[4] H. R. Pruppacher and J. D. Klett, *Microphysics of Clouds and Precipitation*. Kluwer Academic Publishers, 1997.

[5] J. Moran and M. Morgan, *Meteorolgy: the atmosphere and the science of weather*. Prentice-Hall, 5 ed., 1997.

[6] A. Bray, "Theory of phase-ordering kinetics," *Advances in Physics*, vol. 43, pp. 357–459, June 1994.

[7] J. Vollmer, "Phase separation under ultraslow cooling: Onset of nucleation," *J. Chem. Phys.*, vol. 129, pp. 164502–8, Oct. 2008.

[8] M. E. Cates, J. Vollmer, A. Wagner, and D. Vollmer, "Phase separation in binary fluid mixtures with continuously ramped temperature," *Philosophical Transactions of the Royal Society A: Mathematical, Physical and Engineering Sciences*, vol. 361, pp. 793–807, Apr. 2003.

[9] D. Vollmer, R. Strey, and J. Vollmer, "Oscillating phase separation in microemulsions. i. experimental observation," *Journal of Chemical Physics*, vol. 107, no. 9, pp. 3619–3626, 1997.

[10] G. K. Auernhammer, D. Vollmer, and J. Vollmer, "Oscillatory instabilities in phase separation of binary mixtures: Fixing the thermodynamic driving," *J. Chem. Phys.*, vol. 123, pp. 134511–8, Oct. 2005.

[11] J. Vollmer, G. K. Auernhammer, and D. Vollmer, "Minimal model for phase separation under slow cooling," *Physical Review Letters*, vol. 98, p. 115701, Mar. 2007.

[12] D. Vollmer, J. Vollmer, and A. J. Wagner, "Oscillatory kinetics of phase separation in a binary mixture under constant heating," *Physical Chemistry Chemical Physics*, vol. 4, pp. 1380–1385, 2002.

[13] R. S. Sparks, H. E. Huppert, T. Koyaguchi, and M. A. Hallworth, "Origin of modal and rhythmic igneous layering by sedimentation in a convecting magma chamber," *Nature*, vol. 361, pp. 246–249, 1993.

[14] Y. Hayase, M. Kobayashi, D. Vollmer, H. Pleiner, and G. K. Auernhammer, "Asymmetric oscillations during phase separation under continuous cooling: A simple model," *J. Chem. Phys.*, vol. 129, pp. 184109–7, Nov. 2008.

[15] S. Yamaguchi, "Three-phase behavior and the roles of c4e1 in the water/c12e5/c4e1/decane system," *Colloids and Surfaces A: Physicochemical and Engineering Aspects*, vol. 262, pp. 118–124, July 2005.

[16] C. Browarzik, D. Browarzik, and J. Winkelmann, "Modeling of the three-phase equilibrium in systems of the type water + nonionic surfactant + alkane," *Fluid Phase Equilibria*, vol. In Press, Corrected Proof, pp. –.

[17] S. Fowler and P. Greenspan, "Application of nile red, a fluorescent hydrophobic probe, for the detection of neutral lipid deposits in tissue sections: comparison with oil red o," *J. Histochem. Cytochem.*, vol. 33, no. 8, pp. 833–836, 1985.

[18] A. Cser, K. Nagy, and L. Biczók, "Fluorescence lifetime of nile red as a probe for the hydrogen bonding strength with its microenvironment," *Chemical Physics Letters*, vol. 360, pp. 473–478, July 2002.

[19] H. Nakayama, H. Kanenaga, and T. Fujioka, "The study of water structure in aqueous solutions of butoxyethanol by enthalpy of mixing measurements," *Journal of Thermal Analysis and Calorimetry*, vol. 64, pp. 193–199, Apr. 2001.

[20] J. S. Walker and C. A. Vause, "Wiederkehrende phasen," *Spektrum der Wissenschaft*, p. 86ff, 1987.

[21] H. Doi, K. Tamura, and S. Murakami, "Thermodynamic properties of aqueous solution of 2-isobutoxyethanol at t = (293.15, 298.15, and 303.15) k, below and above lcst," *The Journal of Chemical Thermodynamics*, vol. 32, pp. 729–741, June 2000.

[22] R. C. Weast, *CRC Handbook of Chemistry and Physics*. CRC Press, Inc. Boca Raton, Florida, 69. ed., 1988-1989.

[23] K. Menzel, S. Z. Mirzaev, and U. Kaatze, "Crossover behavior in micellar solutions with lower critical demixing point: Broadband ultrasonic spectrometry of the isobutoxyethanol-water system," *Phys. Rev. E*, vol. 68, p. 011501, July 2003.

[24] G. Batchelor, *An Introduction to Fluid Dynamics*. Cambridge University Press, 2005.

[25] H. G. Maas, A. Gruen, and D. Papantoniou, "Particle tracking velocimetry in three-dimensional flows," *Experiments in Fluids*, vol. 15, no. 2, pp. 133–146, 1993.

[26] N. A. Malik, T. Dracos, and D. A. Papantoniou, "Particle tracking velocimetry in three-dimensional flows," *Experiments in Fluids*, vol. 15, no. 4, pp. 279–294, 1993.

[27] N. Ouellette, H. Xu, and E. Bodenschatz, "A quantitative study of three-dimensional lagrangian particle tracking algorithms," *Experiments in Fluids*, vol. 40, no. 2, pp. 301–313, 2006.

[28] J. H. J. Thijssen and P. S. Clegg, "Emulsification in binary liquids containing colloidal particles: a structure-factor analysis," *Journal of Physics: Condensed Matter*, vol. 22, no. 45, p. 455102, 2010.

[29] B. P. Binks, "Particles as surfactants–similarities and differences," *Current Opinion in Colloid & Interface Science*, vol. 7, pp. 21–41, Mar. 2002.

[30] C.-O. Fournier, L. Fradette, and P. Tanguy, "Effect of dispersed phase viscosity on solid-stabilized emulsions," *Chemical Engineering Research and Design*, vol. 87, pp. 499–506, Apr. 2009.

[31] I. J. Benczik and J. Vollmer, "A reactive-flow model of phase separation in fluid binary mixtures with continuously ramped temperature," *EPL (Europhysics Letters)*, vol. 91, no. 3, pp. 36003–, 2010.

[32] S. Maass, J. Grünig, and M. Kraume, "Measurement techniques for drop size distributions in stirred liquid-liquid systems," *Chemical and Process Engineering*, vol. 30, pp. 635–651, 2009.